FUN3D Mesh Adaptation Simulations of 4th AIAA High-Lift Prediction Workshop Case 1a

Stephen L. Wood* and Michael A. Park†
NASA Langley Research Center, Hampton, VA 23681, USA

This paper describes in detail the FUN3D Mesh adaptation simulation results for Case 1a of the 4th AIAA High-Lift Prediction Workshop (HLPW-4). The Stabilized Finite Element library with FUN3D is used along with the Negative Spalart-Allmaras One-Equation Model to simulate fully turbulent free-air flow around the High Lift version of the Common Research Model at three flap settings. Meshes are adapted using multi-scale and goal-oriented metrics. The results are presented and the discussion focuses on the predicted differences between the three flap settings. Coefficients of lift, drag, and pitching moment are predicted within 7% of values measured in the QinetiQ 5m Wind Tunnel at each flap setting. Predicted surface pressures and skin friction distributions show inconsistent discrepancies with measurements across the flap settings. Consequently, flap increments for these figures of merit are not well predicted. These predictions are consistent with submissions to the HLPW-4 from other RANS-SA methods. Visualizations of Liutex vortex cores colored by angular velocity are presented as possible new quantitative and qualitative perspective for solution evaluation.

I. Introduction

The 4th AIAA High-Lift Prediction Workshop (HLPW-4) examines the NASA 10% scale, semispan model configuration (CRM-HL) [1] in the QinetiQ 5m Wind Tunnel [2, 3]. The goals of the HLPW series are to assess the numerical prediction capability of current-generation [Computational Fluid Dynamics] CFD technology/codes for swept, medium-to-high-aspect ratio wings for landing/take-off (high-lift) configurations. Develop practical modeling guidelines for CFD prediction of high-lift flow fields. Determine the elements of high-lift flow physics that are critical for modeling to enable the development of more accurate prediction methods and tools. Enhance CFD prediction capability for practical high-lift aerodynamic design and optimization [4]. In order to improve the state-of-the-art in computational fluid dynamics, Langley Research Center and Ames Research Center joined forces to produce data sets using the same research model–the Common Research Model [5].

Case 1a of HLPW-4 focuses on three inboard/outboard TE flap deflections (37°/34°, 40°/37°, and 43°/40°) with the purpose of determine ability of CFD to predict force and moment increments for three flap deflections at a nominal angle-of-attack. In this paper, the Stabilized Finite Element library with FUN3D, is used along with the Negative Spalart-Allmaras One-Equation Model to simulate fully turbulent flow around the CRM-HL. The Sketch-to-Solution process [6, 7] is used to generate meshes comprised completely of tetrahedra. The first ten automatically adapted meshes are intended to control interpolation error of the Mach number field and the following eight meshes controlled the error in the drag coefficient. This staged use of mesh metrics is based upon the lessons learned conducting simulations of the Juncture Flow Model on expert-crafted and adapted meshes [8], and while conducting an angle-of-attack sweep for high lift configurations [9]. Adaptations are done using the concept of mesh-metric duality [10], which is particularly suitable for generating highly anisotropic meshes. An excellent review of metric-based mesh adaptations is given by Alauzet et al. [11]. Here, metric field tensors are used to describe the desired meshes, and a metric-conforming mesh generator is used to generate the meshes from the metric fields. For the presented results, *refine* [12] is used as the metric-conforming mesh generator.

For adaptations where interpolation error is controlled, the approach by Loseille et al. [13] is used, whereas for those where output error is controlled, the methodology described in Ref. [14] has been implemented. Both of these appoaches have been verified in [15] and [16].

*Research Scientist, Computational AeroSciences Branch, AIAA Senior Member, stephen.l.wood@nasa.gov.
†Research Scientist, Computational AeroSciences Branch, AIAA Associate Fellow.

II. Numerical Methods and Problem Setup

The FUN3D/SFE CFD code, turbulence model, and mesh generation methods are briefly described. The flow conditions are also given.

A. FUN3D/SFE

FUN3D/SFE is a continuous finite-element discretization within FUN3D [17, 18]. The discretization is a stabilized finite-element approach based on the Streamlined Upwind Petrov-Galerkin (SUPG) scheme [19, 20]. For turbulent flows, the SA-neg [21, 22] is tightly coupled with the mean flow equations, yielding a nonlinear algebraic system of equations with six variables at each mesh point. A pressure gradient smoother based upon the Exponential-Entropy Gradient Sensor described by Holst et al. [23], is used to facilitate robust physical solutions on adapted meshes where increasing resolution often reveals new interactions with geometry and between flow structures. A linear nodal basis is used in this study, which is designed to be second-order accurate in space. The current implementation includes capabilities for computing on tetrahedra, hexahedra, pyramids, and prisms. FUN3D/SFE is used to perform forward CFD analysis as well as adjoint analysis [24, 25], which is required for goal-oriented adaptation. Forward CFD analysis and adjoint analysis use real-values in double (64 bit) precision, to represent the domain, initial conditions, and solution [18].

To advance the solution toward a steady state, the density, velocities, temperature, and the turbulence working variable are updated in a tightly-coupled Newton-Krylov-type solver described in Ref. [18]. Here, an initial update to the flow variables is computed using a locally varying pseudotime-step parameter that is multiplied by the current Courant–Friedrichs–Lewy (CFL) number. The CFL number is adjusted during the iterative process according to a controller based upon the alpha controller described in Ref. []. During each iteration of the nonlinear solver, the Spare Linear Algebra Toolkit (SLAT) is used to solve the linear system using a Generalized Minimal Residual (GMRES) [26] method right-preconditioned with an Incomplete Lower-Upper approximate solve [26]. If GMRES does not find a solution that meets the convergence criteria (absolute = 10^{-14}, relative = 10^{-8}), any partitions of the MPI distributed preconditioners that amplified the $L2$ norm of a Krylov search vector by more than 10^{10} are reordered dynamically [27], and the linear solve is retried.

The adjoint solution is a set of costate-variables, λ, for a particular output functional, I, obtained by solving the linear system of equations,

$$\left[\frac{\partial R_h}{\partial q_h}\right]^T \lambda = -\left(\frac{\partial I}{\partial q_h}\right)^T \quad , \tag{1}$$

where q_h is the set of solution state variables, and R_h is the discrete residual of the partial differential equations under consideration [25, 28]. The linear solver and preconditioner operations are stress-tested by the numerical stiffness of adjoint systems. These adjoint systems are exceptionally stiff due to an effectively infinite CFL number, which negates the boost to diagonal dominance provided by the pseudotime term.

Two parallelization strategies are used to produce the solutions in this work. 1) All MPI: Computations on each mesh partition are performed with one MPI process using one CPU core. 2) Hybrid(P): Computations on each mesh partition are performed with one MPI process using P CPU cores as OpenMP threads. The All MPI parallelization strategy is used for steady-state forward solutions. The Hybrid(8) parallelization strategy is used for adjoint solutions. A Hybrid(8) parallelization uses eight times fewer mesh partitions as the All MPI parallelization on the same number of CPU cores. Generally, larger partitions improve the efficacy of ILU(k) preconditioners, thereby improving efficiency and robustness. Larger partitions also require less halo data exchange, which reduces MPI communication for an additional efficiency gain. Level scheduling implementations of ILU(k) factorization and application algorithms are used to enable at least 75% weak scaling up to 8 OpenMP threads [29].

B. Adaptation

The *refine* open source mesh-adaptation mechanics package developed by NASA, is currently used as the metric-conforming mesh generator [12]. *refine* is available via NASA's Public GitHub account * under the Apache License. refine accesses the topology and evaluate geometry via the Electronic Geometry Aircraft Design System (EGADS) [30]. EGADS is part of the Engineering Sketch Pad (ESP) [31], which includes the Open-source Constructive Solid Modeler (OpenCSM) [32] for initial geometry import and setup. High-performance computing equipment is supported by EGADSlite [33], a lightweight ANSI-C version of the EGADS functions required by the initial and adaptive mesh process. refine utilizes EGADSlite for efficient parallel execution and geometry evaluation. The multiscale metric used

*https://github.com/NASA/refine

in the present work was originally developed by Loseille et al. [34]. Adapted solutions using the multiscale metric are used to compare with solutions obtained using a goal-oriented metric that will be described later in this section. The multiscale metric aims to control the L^p-norm of the interpolation error of a solution scalar field to target both smooth and unsmooth error contributions. Classic Hessian-based adaptation methods [35, 36] control quadratic interpolation error estimates in the L^∞-norm, which results in excessive refinement of unsmooth regions. Multiscale adaptation is used to generate meshes on the first two complexity levels.

For goal-oriented adaptation of the High Lift Common Research Model (CRM-HL) model [2], *refine* [12] and the viscous metric approach reported by Loseille et al. [14] are utilized. The viscous goal-oriented approach involves the optimization of an a priori error estimate of output functionals for the RANS equations in the continuous mesh framework using calculus of variations, resulting in an analytical formulation for the metric field [37]. The resulting metric field essentially consists of the sum of Hessians of the RANS fluxes, weighted by the gradient components of the adjoint fields [25]. The adjoint fields used in the present work are calculated for the drag coefficient output functional as described in Ref. [29]. Pyrefine, a set of python driver scripts, is used to orchestrate the sequece of CFD jobs and *refine* staged metric mesh adapatations at each flap setting.

C. Flow Conditions

The NASA 10% scale, semispan model configuration [3] QinetiQ 5m Wind Tunnel is used for this case. This configuration was tested at three inboard/outboard TE flap deflections (37°/34°, 40°/37°, and 43°/40°) with a nominal 30°/30° inboard/outboard leading-edge (LE) slat setting, nacelle, pylon, nacelle chine, LE brackets, TE support fairings, but no landing gear, horizontal or vertical tail [2]. The median values from the test of Mach number, $M_\infty = 0.2$, chord Reynolds number, $Re_c = 5.49$ million, and temperature, $T_\infty = 289.444$ K are used along with the wall corrected angle of attack $\alpha = 7.05°$ for free-air computations.

III. Results

The measurements made in the QinetiQ 5m Wind Tunnel are denoted in Tables and Figures by "EXP." Coefficients of Lift (C_L), Drag (C_D), and Pitching Moment (C_{my}) predicted throughout the adaptation process are presented and discussed in Section III.A. Surface pressures from eight workshop defined wing stations in the final simulations are presented and discussed in Section III.B. Off-Body Vorticity Contours are presented along with visualizations of Liutex Vortex cores in Section III.D. Convergence of the forward and adjoint solutions are presented in Section III.E. Lastly, the computational cost paid to generate these results is summarized in Section III.F.

A. Lift, Drag, and Pitching Moment Coefficients

Figures 1a, 1b, and 1c display the lift (C_L), drag (C_D), and pitching moment (C_{my}) coefficients, respectively, throughout the adaptation process. The coefficients shown in the plots are calculated using the FUN3D/SFE method. The multiscale metric is used to concentrate mesh nodes so that large gradients in the Mach field are resolved. Large gradients in the Mach field are commonly found in the near-body and wake region of wing-bodies. The goal-oriented metric derived from the drag cost function emphasizes resolution of regions influential to drag force. In subsonic flows, regions upstream of wing-bodies, where the bow-wave extends to the free-stream, contain nascent entrainment regions that envelop downstream boundary layers [8, 38–40]. The impact of impulsively changing the mesh adaptation metric from multiscale goal-oriented between mesh 11 and 12 is easily visible in Figure 1b. Following the impulsive change in metric, the number of nodes in the mesh for each flap setting initially decreases to better conform with the adjoint drag cost function metric. After the initial decrease, the number of nodes in each mesh increases as conformity can be balanced across the bow-wave, near-body, and wake regions.

Table 1 summarizes the coefficients of C_L, C_D, and C_{my} predicted on the last adapted mesh. The context provided by the experimental values in Figure 1 and Table 1 indicates that the predictions of these figures of merit (FOM) are accurate within 7% of values measured in the QinetiQ experiment [2, 3]. However, the increments in these FOM are not well predicted. The most accurate increment predictions are ΔC_L 40°/37°- 43°/40°and ΔC_L 40°/37°- 37°/34°, which underpredict the impact by 5.8% and 14%, respectively.

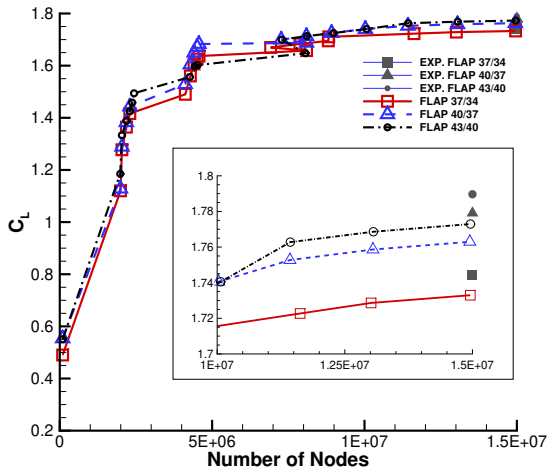

(a) Lift

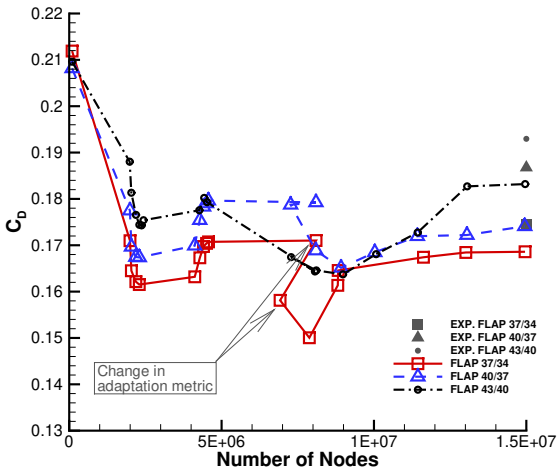

(b) Drag

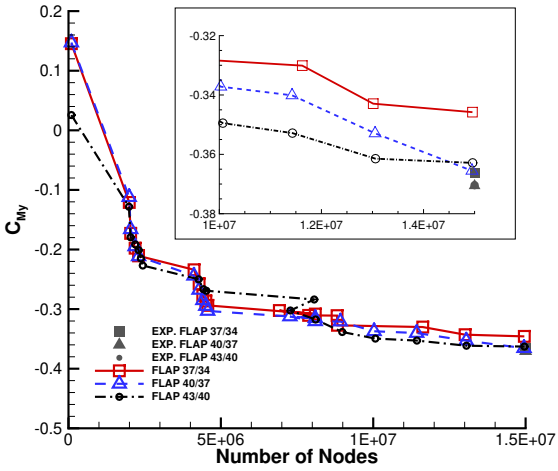

(c) Pitching Moment

Fig. 1 Figures of Merit predicted on adapted meshes for each flap setting.

Table 1 Figures of merit from experiment and CFD at each flap setting, the change between flap settings, and the relative errors between experiment and CFD.

	Experiment	CFD	% Rel. Error
Flap 37°/34°			
C_L	1.7442	1.73296	0.64446
C_D	0.17438	0.16860	3.31550
C_{my}	-0.36616	-0.34579	5.56389
Flap 40°/37°			
C_L	1.77908	1.76296	0.90584
C_D	0.18676	0.17409	6.78152
C_{my}	-0.37057	-0.36552	1.36243
Flap 43°/40°			
C_L	1.78965	1.77292	0.93469
C_D	0.19296	0.1832	5.05897
C_{my}	-0.37039	-0.36287	2.02932
Δ (40°/37°- 37°/34°)			
C_L	0.03487	0.03000	13.97849
C_D	0.01238	0.00550	55.60250
C_{my}	-0.00441	-0.01973	-347.483
Δ (40°/37°- 43°/40°)			
C_L	-0.01057	-0.00996	5.78882
C_D	-0.00620	-0.00910	-46.8285
C_{my}	-0.00018	-0.00265	-1370.91

B. Surface Pressure

Surface pressure coefficient comparisons on the slats, wing, and flaps at eight spanwise locations are shown in Figures 2– 9. The first subfigure in each of these figures depicts the location where surface pressures are extracted from the final adapted meshes for each flap setting. These locations approximate the planes where pressure taps were located in the QinetiQ experiment [2–4]. The subsequent subfigures depict the pressure coefficients measured in the experiemnt with symbols and those extracted from the final adapted meshes with lines on the slats (when present), wing, and flaps (when present).

Figure 2 depicts the pressure coefficients measured at Station A. Subfigures 2b and 2c show small differences in the measured pressures between the flap settings. Pressures on the suction side of the slat and wing at Station A are underpredicted. Pressures on the pressure side of the slat are slightly overpredicted while pressures on the pressure side of the wing and flap are well predicted. Subfigure 2d depicts significant differences in the flap suction peak at the three flap settings. The suction peaks for 37°/34° and 40°/37° flap settings are predicted in good agreement with measurements, however, the 43°/40° suction peak is predicted at the same level as 40°/37°.

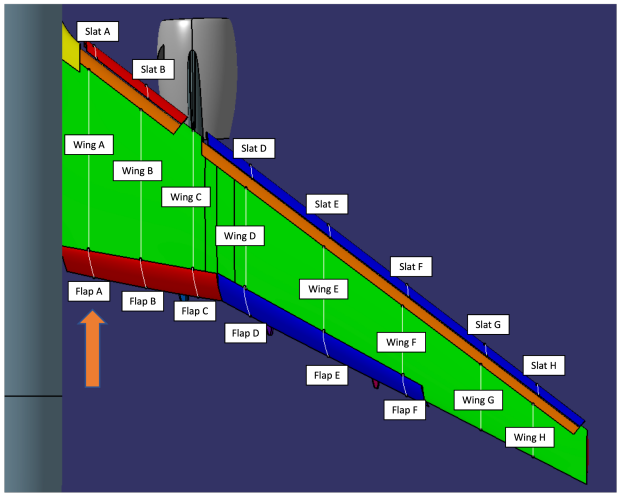

(a) Station A [4]

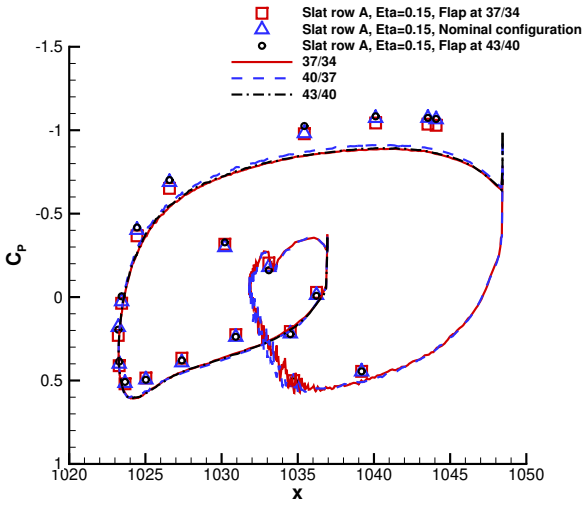

(b) Slat A

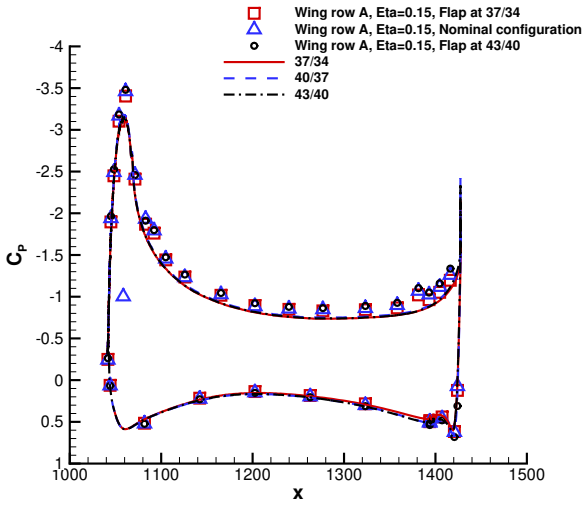

(c) Wing A

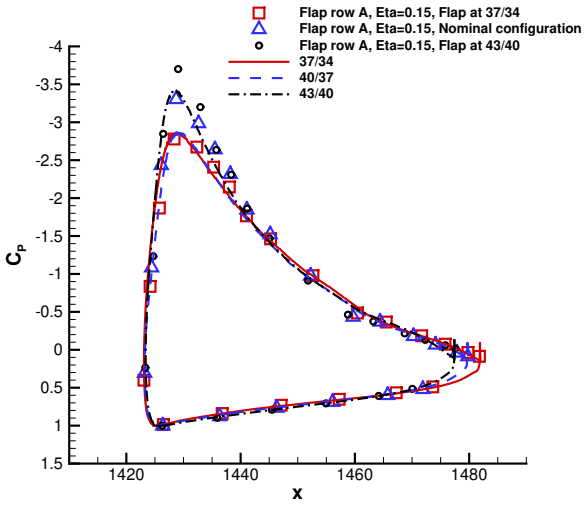

(d) Flap A

Fig. 2 Surface pressure coefficients extracted at station A.

Figure 3 depicts the pressure coefficients measured at Station B. Subfigures 3b and 3c show small differences in the measured pressures between the flap settings. Pressures on the suction side of the slat and wing at Station B are underpredicted. Pressures on the pressure side of the slat are slightly overpredicted while pressures on the pressure side of the wing and flap are well predicted. Subfigure 3d depicts significant differences in the flap suction peak at the three flap settings. The predicted suction peak for 37°/34° is in good agreement with measurements, however, the 40°/37° suction peak is underpredicted, and the 43°/40°suction peak is overpredicted.

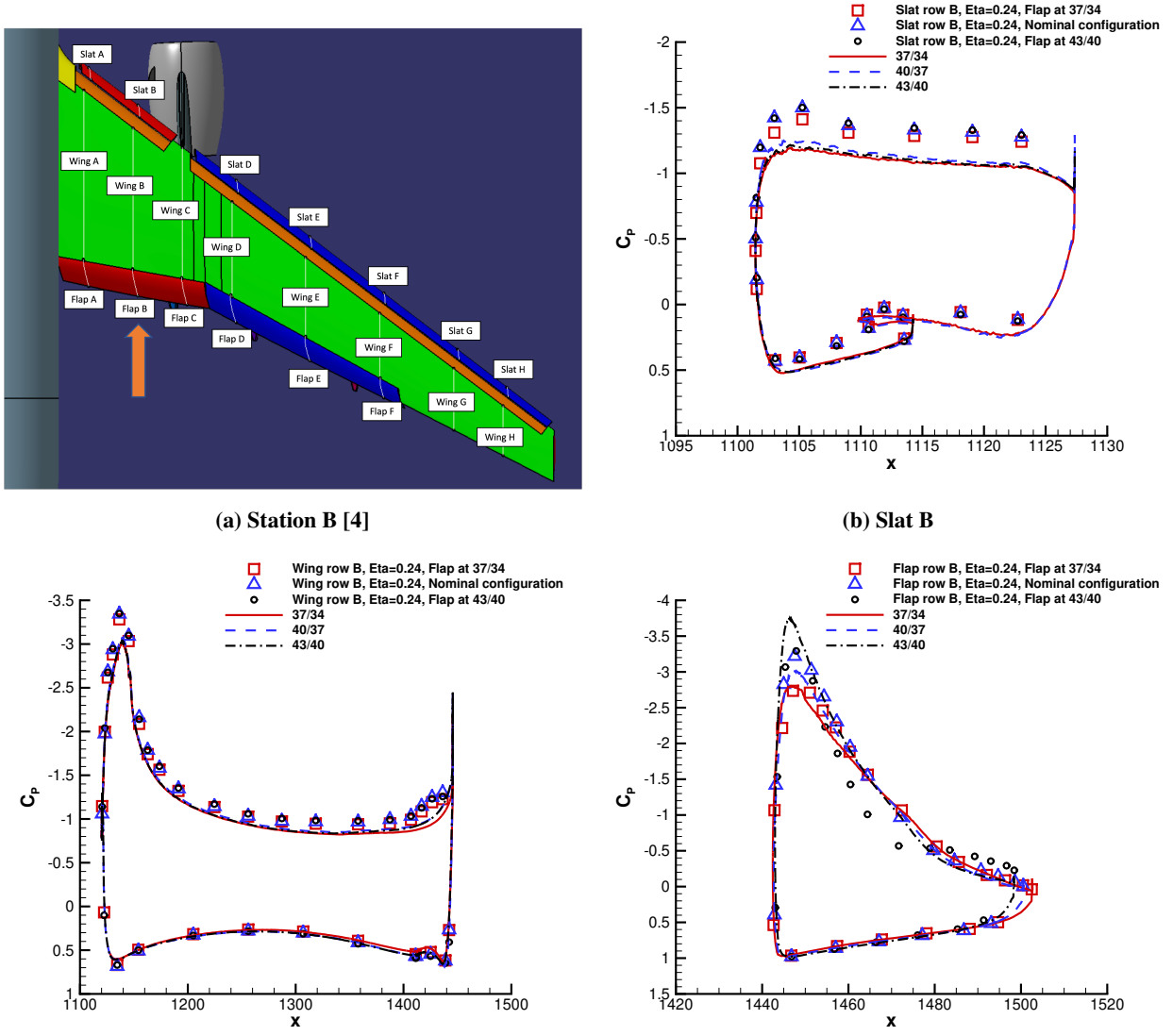

(a) Station B [4]

(b) Slat B

(c) Wing B

(d) Flap B

Fig. 3 Surface pressure coefficients extracted at station B.

Figure 4 depicts the pressure coefficients measured at Station C. Subfigure 4b shows small differences in the measured pressures on the wing between the flap settings. Pressures on the suction side of the wing at Station C are underpredicted, particularly at the trainling edge. No pressures were measured on the pressure side of the wing. Subfigure 4c depicts significant differences in the flap suction peak at the three flap settings. The flap suction peaks for 37°/34°, 40°/37°, and 43°/40° are underpredicted.

Figure 5 depicts the pressure coefficients measured at Station D. Subfigures 5b and 5c show small differences in the measured pressures between the flap settings. Pressures on the suction side of the slat and wing at Station D are

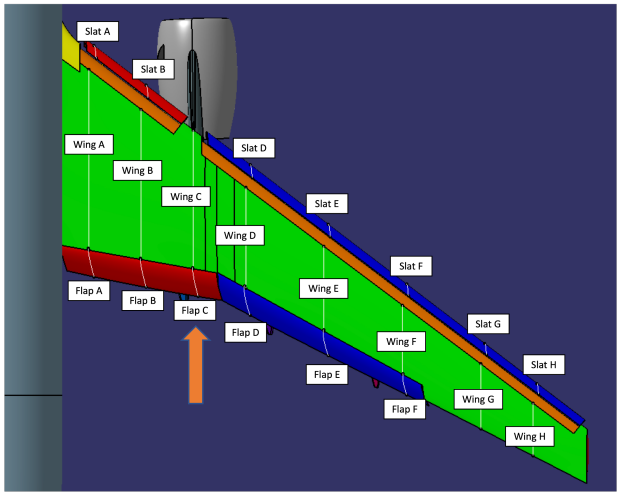

(a) Station C [4]

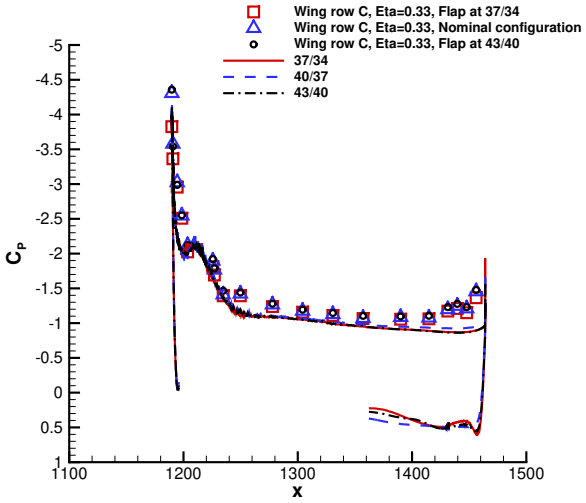

(b) Wing C

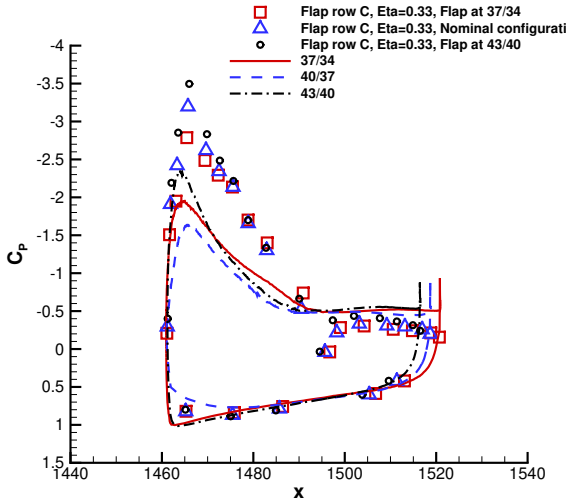

(c) Flap C

Fig. 4 Surface pressure coefficients extracted at station C.

underpredicted. Pressures on the pressure side of the slat, wing, and slat are in good agreement with measurements. Subfigure 5d depicts significant differences in the flap suction peak at the three flap settings. The suction peak for 37°/34° is predicted in good agreement with measurements, however, the suction peaks at 40°/37° and 43°/40° are underpredicted.

Figure 6 depicts the pressure coefficients measured at Station E. Subfigure 6c shows small differences in the pressures measured on the wing between the flap settings. Pressures on the suction side of the slat and wing at Station E are underpredicted particularly at the leading and trailing edges. Pressures on the pressure side of the slat are slightly overpredicted. While pressures on the pressure side of the wing and flap are well predicted. Subfigure 6d depicts significant differences in the flap suction peak at the three flap settings. The flap suction peak is underpredicted for 40°/37°. The predicted flap suction peaks for 37°/34° and 43°/40° are in good agreement with measurements, however, the pressure recovery is predicted to be more rapid than measured.

Figure 7 depicts the pressure coefficients measured at Station F. Subfigure 7c shows small differences in the pressures measured on the wing between the flap settings. Pressures on the suction side of the slat and wing are underpredicted

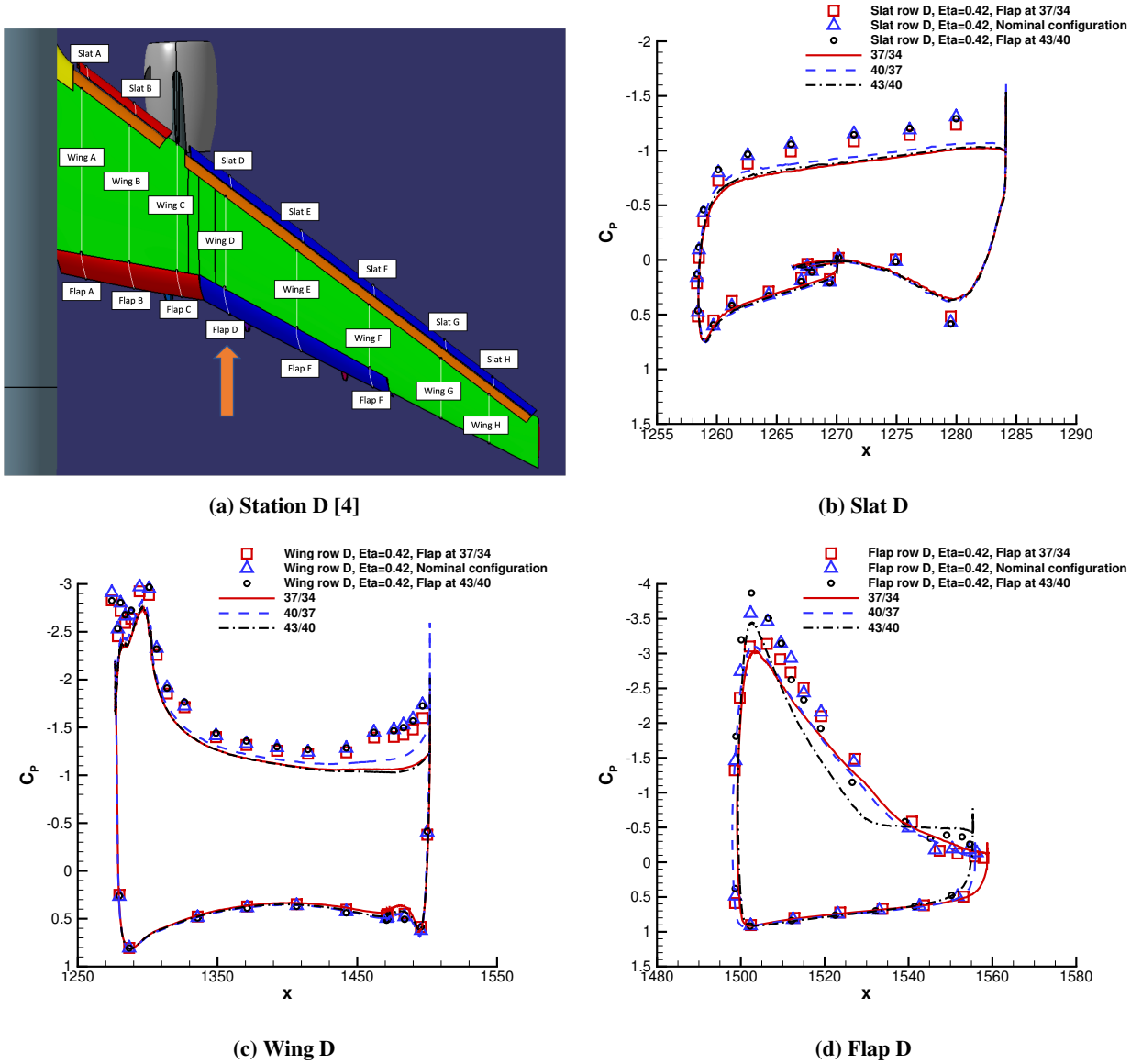

(a) Station D [4]

(b) Slat D

(c) Wing D

(d) Flap D

Fig. 5 Surface pressure coefficients extracted at station D.

particularly at the leading and trailing edges. While pressures on the pressure side of the slat, wing, and flap are well predicted. Subfigure 7d depicts significant differences in the flap suction peak at the three flap settings. The predicted flap suction peaks for 37°/34°, 40°/37°, and 43°/40° collapse to a common value that underpredicts the measurements. The predicted pressure recovery at 43°/40° is significantly more rapid than measured.

Figure 8 depicts the pressure coefficients measured at Station G. Subfigures 8b and 8c show small differences in the pressures measured on the slat and wing between the flap settings, respectively. Pressures on the suction side of the slat are underpredicted at 37°/34° and 43°/40°, while the suction peak is in good agreement with measurements at 40°/37°. Pressures on the pressure side of the slat and wing are well predicted. The initial wing suction peak is predictied in agreement with measurements, however, the pressure recovery is under predicted.

Figure 9 depicts the pressure coefficients measured at Station H. Subfigures 9b and 9c show small differences in the pressures measured on the slat and wing between the flap settings, respectively. Pressures on the suction side of the slat are underpredicted at all three flap settings. Pressures on the pressure side of the slat are well predicted. The initial wing suction peak is predictied in agreement with measurements, however, the pressure recovery is under predicted. Pressures

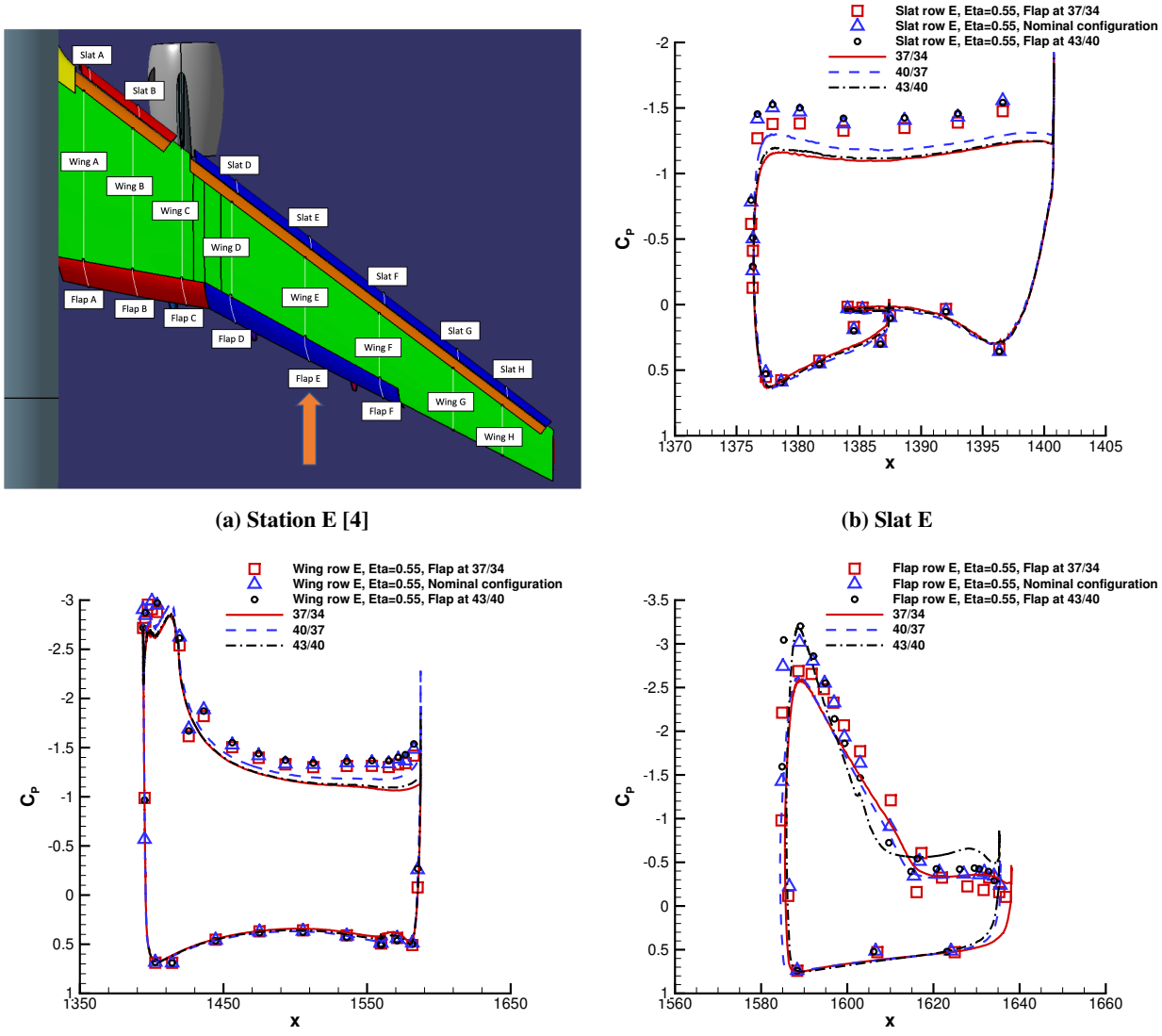

(a) Station E [4]

(b) Slat E

(c) Wing E

(d) Flap E

Fig. 6 Surface pressure coefficients extracted at station E.

on the pressure side of the wing are overpredicted at the leading edge but in good agreement with measurements along the majority of the chord.

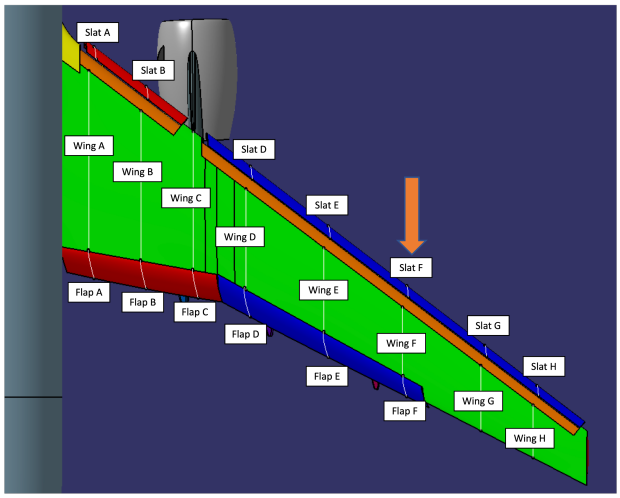

(a) Station F [4]

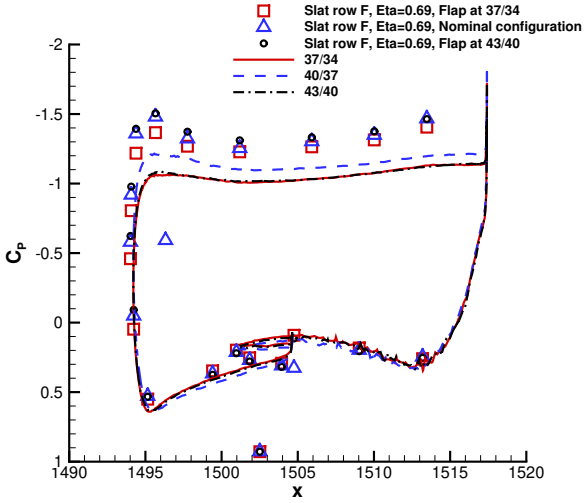

(b) Slat F

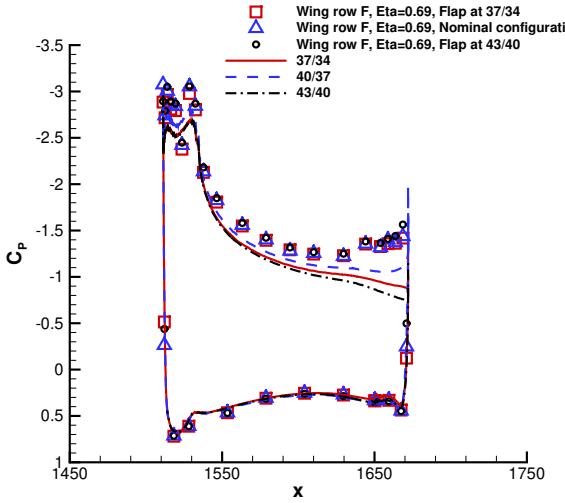

(c) Wing F

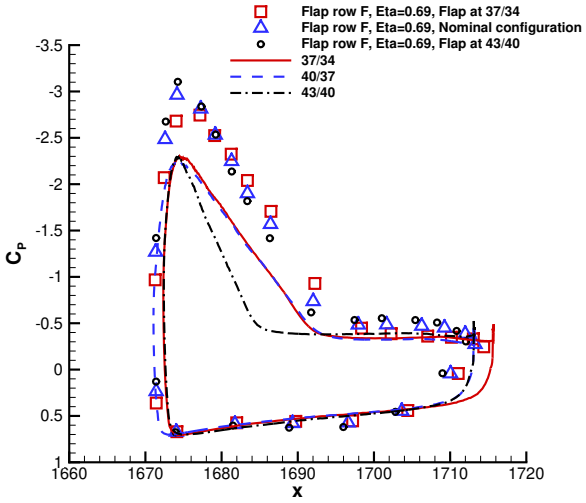

(d) Flap F

Fig. 7 Surface pressure coefficients extracted at station F.

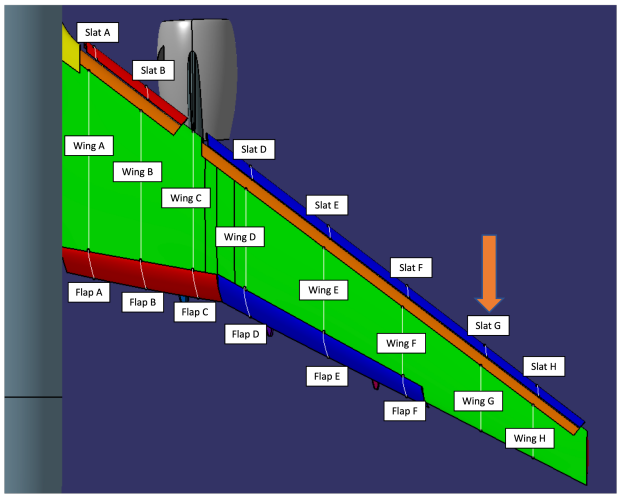

(a) Station G [4]

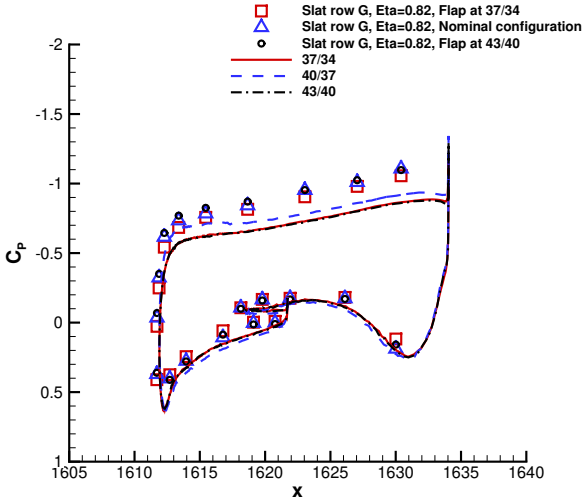

(b) Slat G

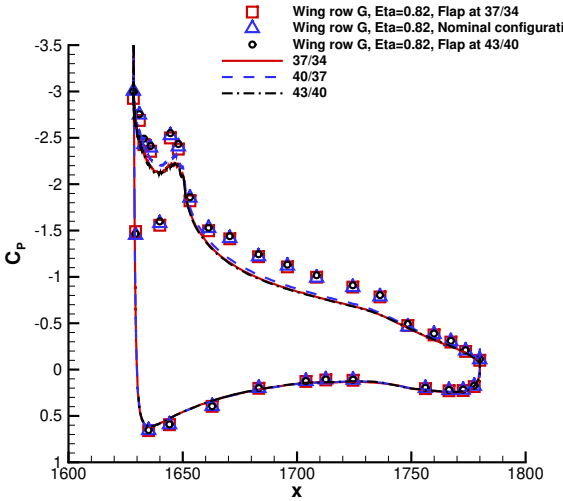

(c) Wing G

Fig. 8 Surface pressure coefficients extracted at station G.

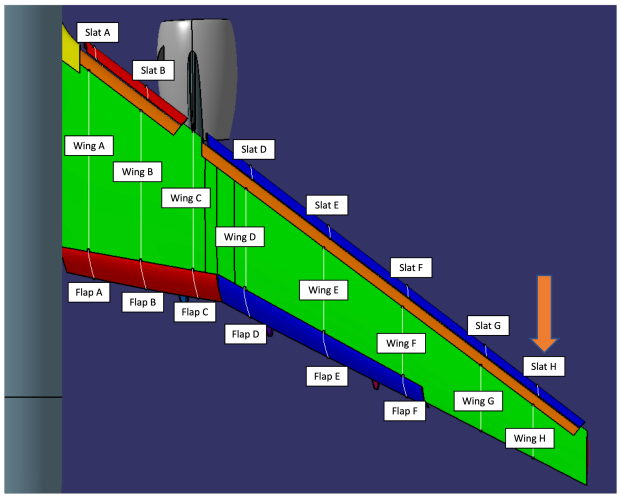

(a) Station H [4]

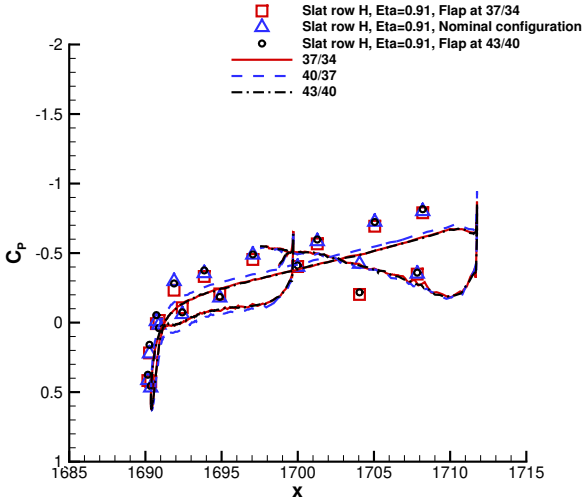

(b) Slat H

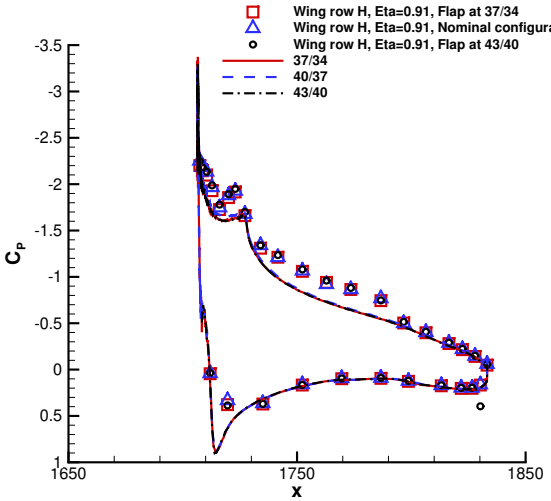

(c) Wing H

Fig. 9 Surface pressure coefficients extracted at station H.

C. Surface Skin Friction Predictions

Five views of skin friction at each flap setting are presented in Figures 10– 14 to identify surface flow patterns and separated regions on the upper surface of the CRM-HL. These views and the color map are standardized to facilitate code-to-code comparison [4]. The values of skin friction shown in these plots are calculated using the FUN3D Finite Volume method and nodal flow state values calculated using the FUN3D Stabalized Finite Element method. The entire wing upper surface can be seen from directly above in Figure 10. Comparing the subplots of Figure 10 reveals the differences in skin friction patterns between the flap settings are concentrated near the trailing edge of the wing and on the flaps.

Figure 11 enlarges the view of the wing root, inboard slat, inboard flap, and nacelle. The imprint of vortices generated by the inboard slat edge, nacelle chine, and pylon appear very similar at all three flap settings. The region of low skin friction on the wing outboard of the imprint of the pylon vortex enlarges as the flap setting increases. The separation region on the inboard flap adjacent to the wing-root extends further outboard as the flap setting increases.

Figure 12 depicts a view focused on the wing, outboard slat, and outboard flap. In this view, the imprint of slat bracket wakes in the skin friction contours diminishes as the flap setting increases. Also visible in this view, the wedge-shaped separation adjacent to the outboard flap's inboard fairing widens towards the inboard flap as the flap setting increases.

Figure 13 depicts a view focused on the outboard ends of the wing, outboard slat, and outboard flap. The imprints of slat bracket wakes and and tip vortices emanating from the outboard slat and wing appear very similar across the flap settings. The imprint of the tip vortices associated with the outboard edge of the outboard flap and the adjacent edge of the wing diminish on the upper flap surface as the flap settings are increased.

Figure 14 depicts a veiw of both flaps, the wing-root, and nacelle, seen from above and behind, looking forward. This perspective provides the clearest view of skin friction patterns associated with separated flow regions on the flaps. As the flap settings are increased, separated regions adjacent to the wing root, and the inboard fairing of the outboard flap grow spanwise. However, the midspan region of the outboard flap shows increases in skin friction as flap settings are increased. The outboard edge of the outboard flap also shows an increase in skin frction from $37°/34°$ to $40°/37°$ and a decrease in skin friction indicative of separation from $40°/37°$ to $43°/40°$.

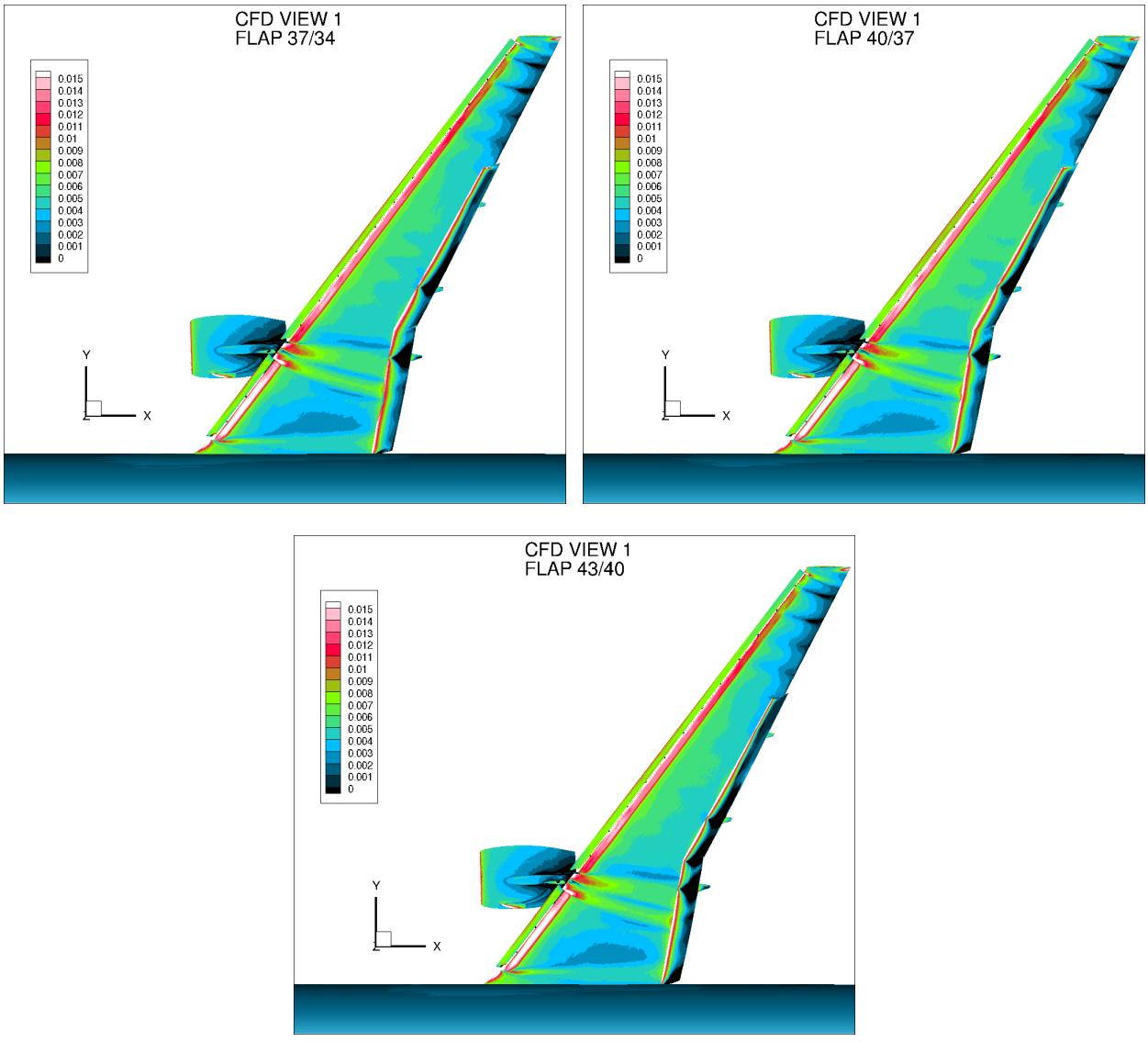

Fig. 10 Contours of surface skin friction coefficient from CFD View 1 [4].

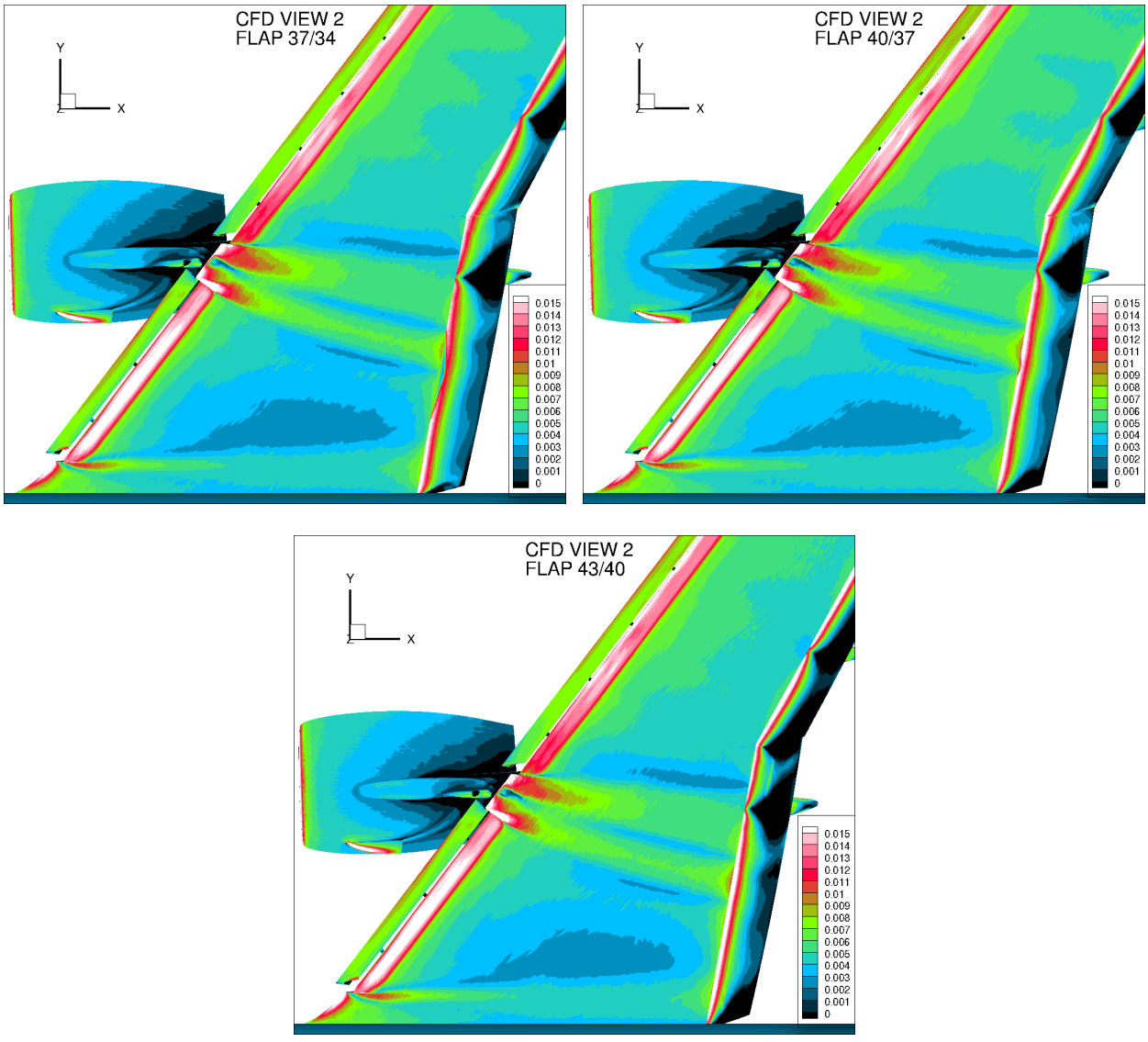

Fig. 11 Contours of surface skin friction coefficient from CFD View 2 [4].

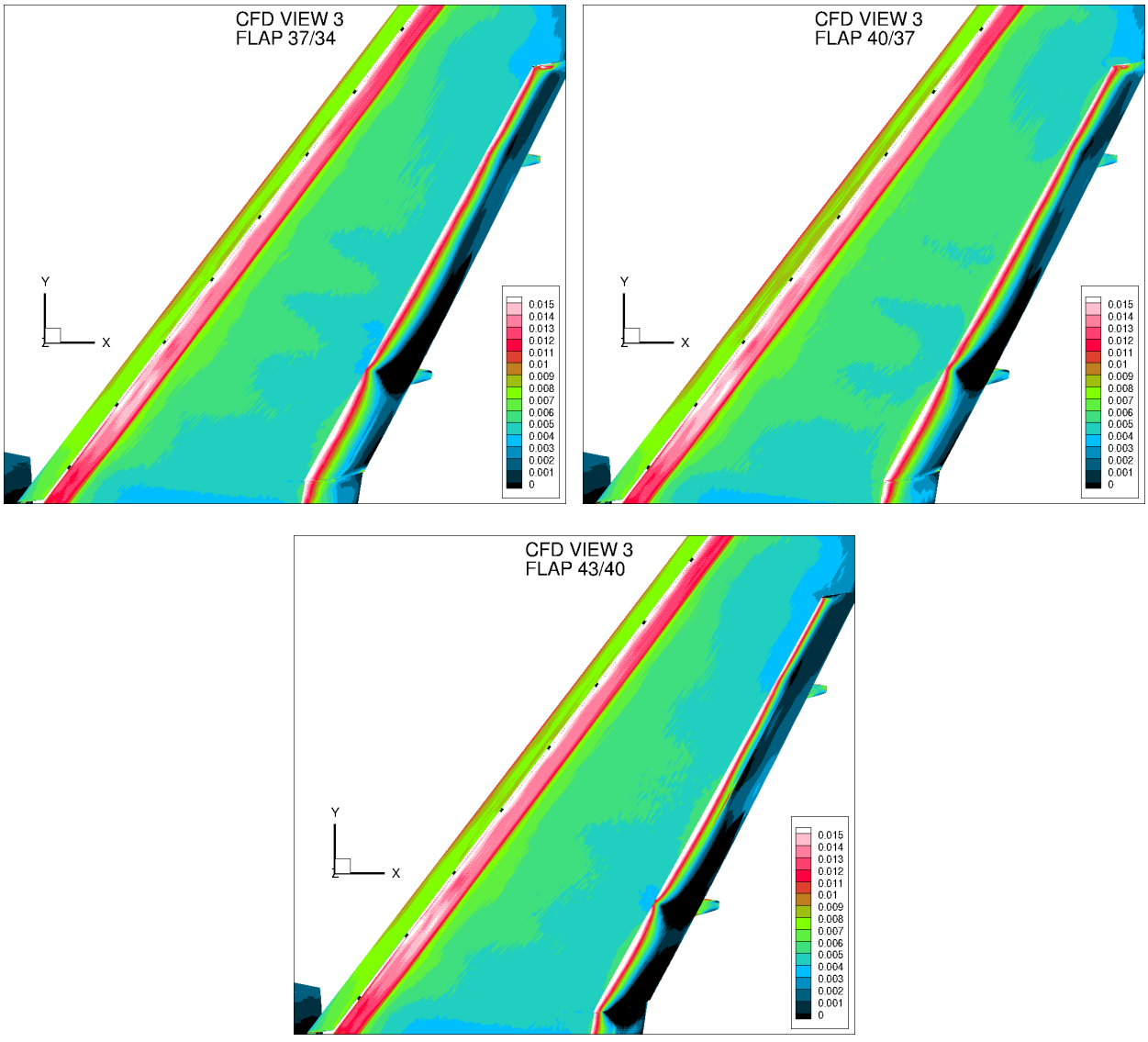

Fig. 12 Contours of surface skin friction coefficient from CFD View 3 [4].

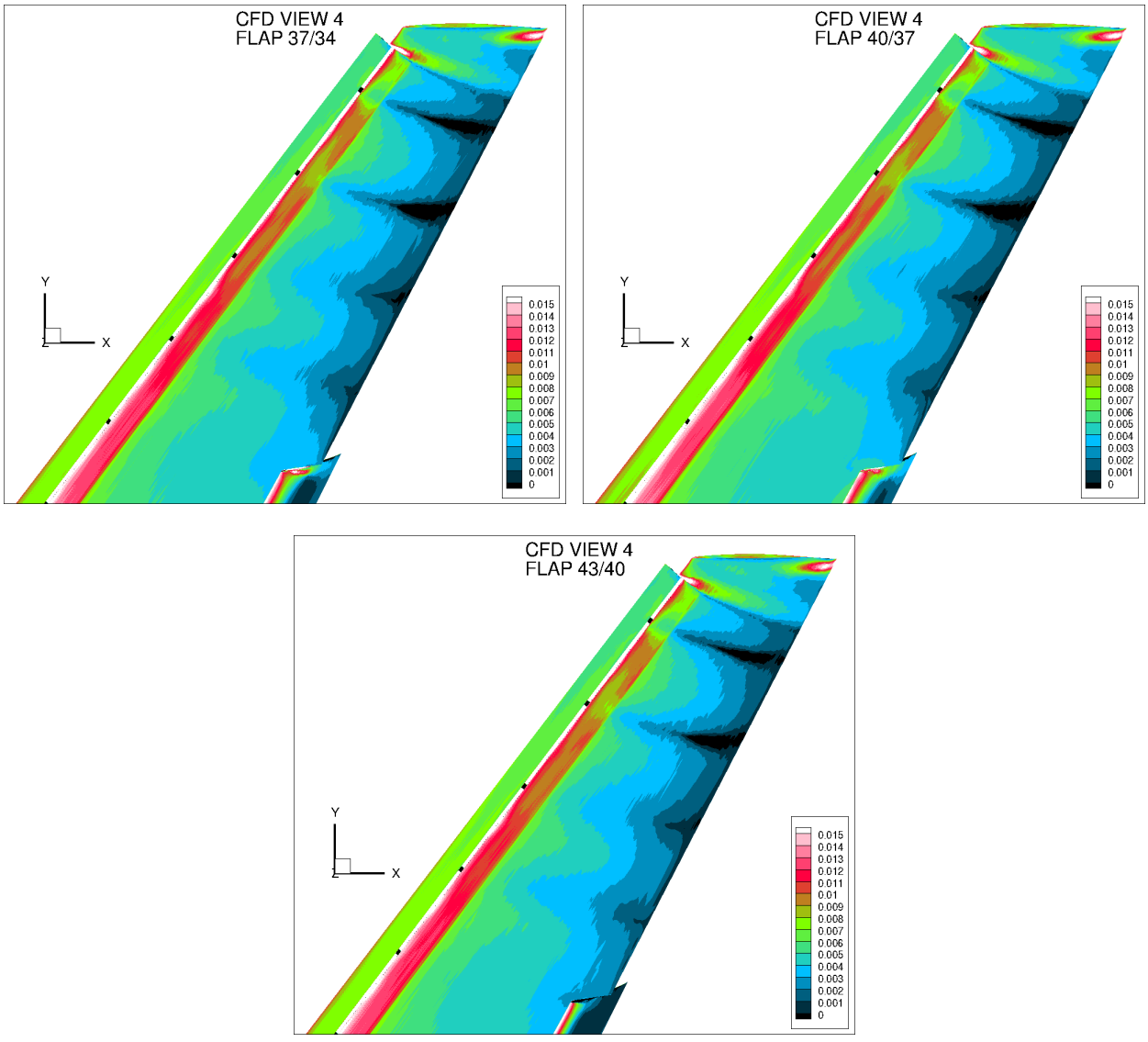

Fig. 13 Contours of surface skin friction coefficient from CFD View 4 [4].

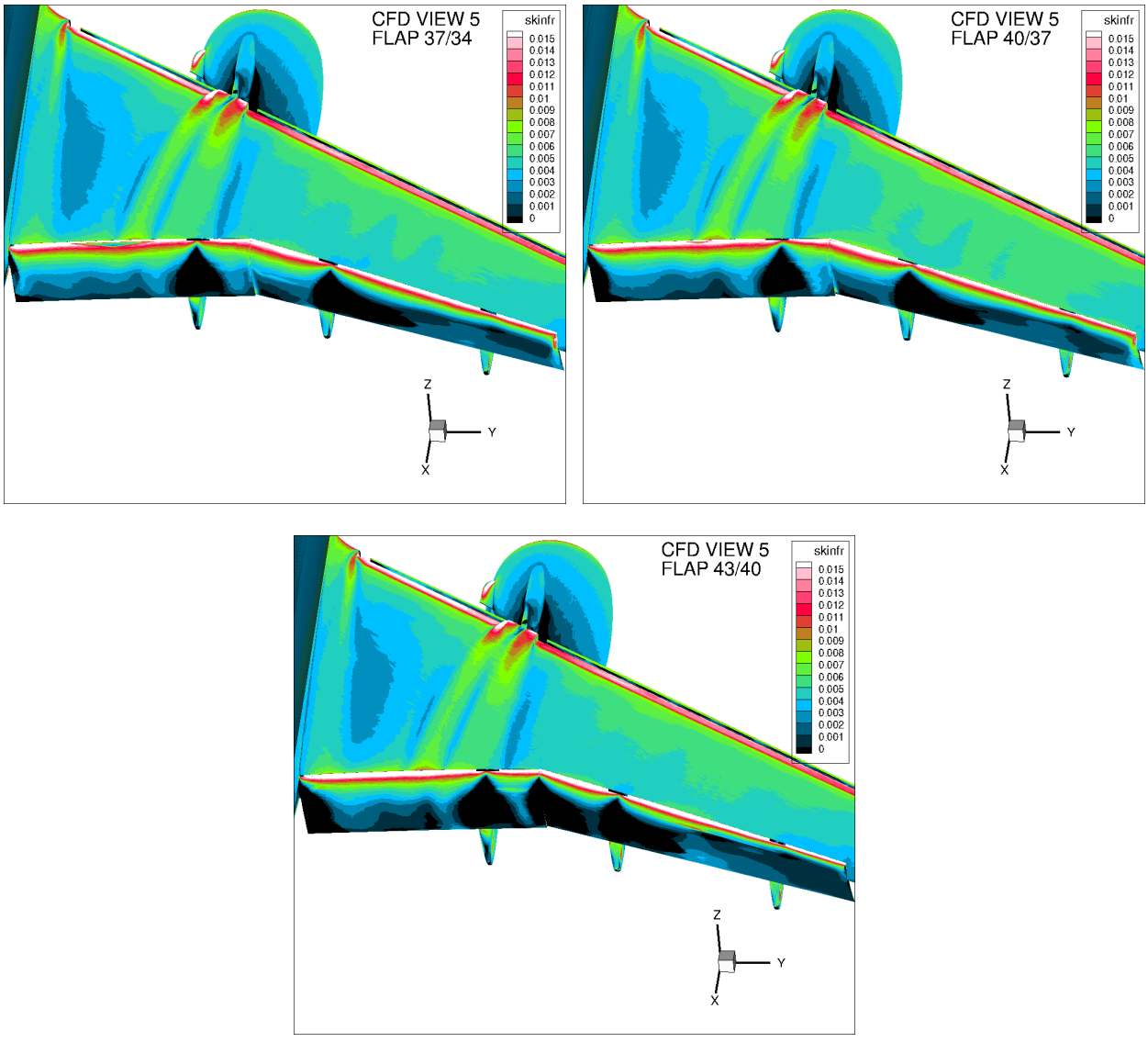

Fig. 14 Contours of surface skin friction coefficient from CFD View 5 [4].

D. Off-Body Vorticity Contours

Five views of vorticity magnitude on x-planes at each flap setting are presented in Figures 15, 16, 17, 18, and 19 to identify vortices around the CRM-HL. These views and the color map are standardized to facilitate code-to-code comparison [4]. The vortex systems that surround wing-body configurations have a significant influence on the downstream flow, including the levels of wall shear stress and separation patterns [38–40].

Only subtle differences in the location and intensity of vorticity magnitude are visible on the planes depicted in Figures 15– 17 across the flap settings. The changes in circulation patterns around the wing as the flap settings are increased are difficult to infer from these data presented in these views.

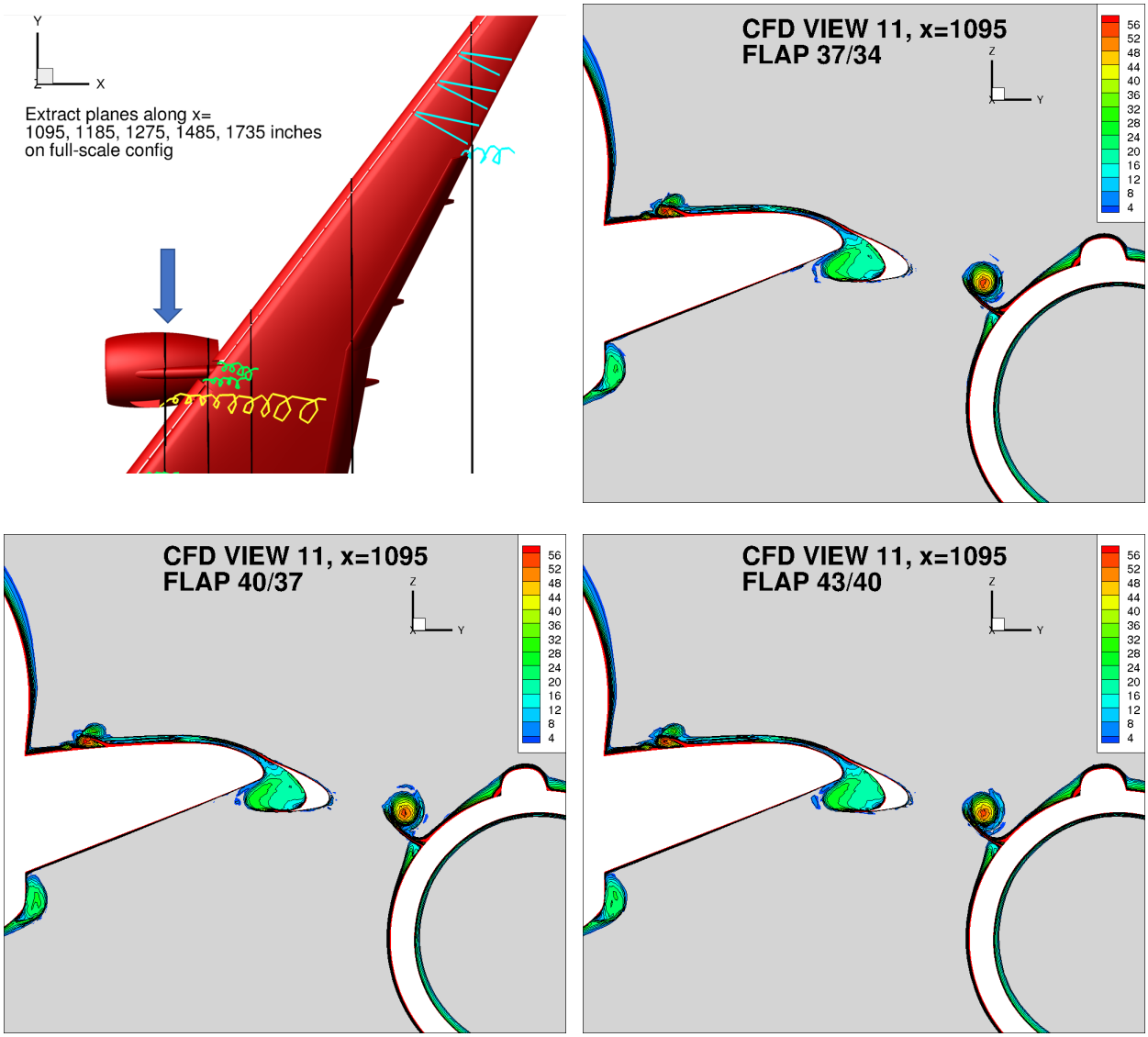

Fig. 15 Nondimensional magnitude of vorticity contours from CFD View 11 [4].

Figure 18 depicts regions adjacent to the inboard edge of the inboard flap and above its inboard fairing where the vorticity magnitude intensifies as the flap settings are increased. This is consistent with the skin friction distribution changes in Figure 14 that also indicate growing separations in these regions. Figure 19 depicts a plane that slices through the wing and outboard flap. On this plane, the imprint of slat bracket wakes on vorticity magnitude appears steady as the flap settings are increased. The vorticity magnitude distributions associated with the outboard edge of the outboard flap and the adjacent wing edge are similar in at 37°/34° and 40°/37°, but appear significantly diminished on this plane at

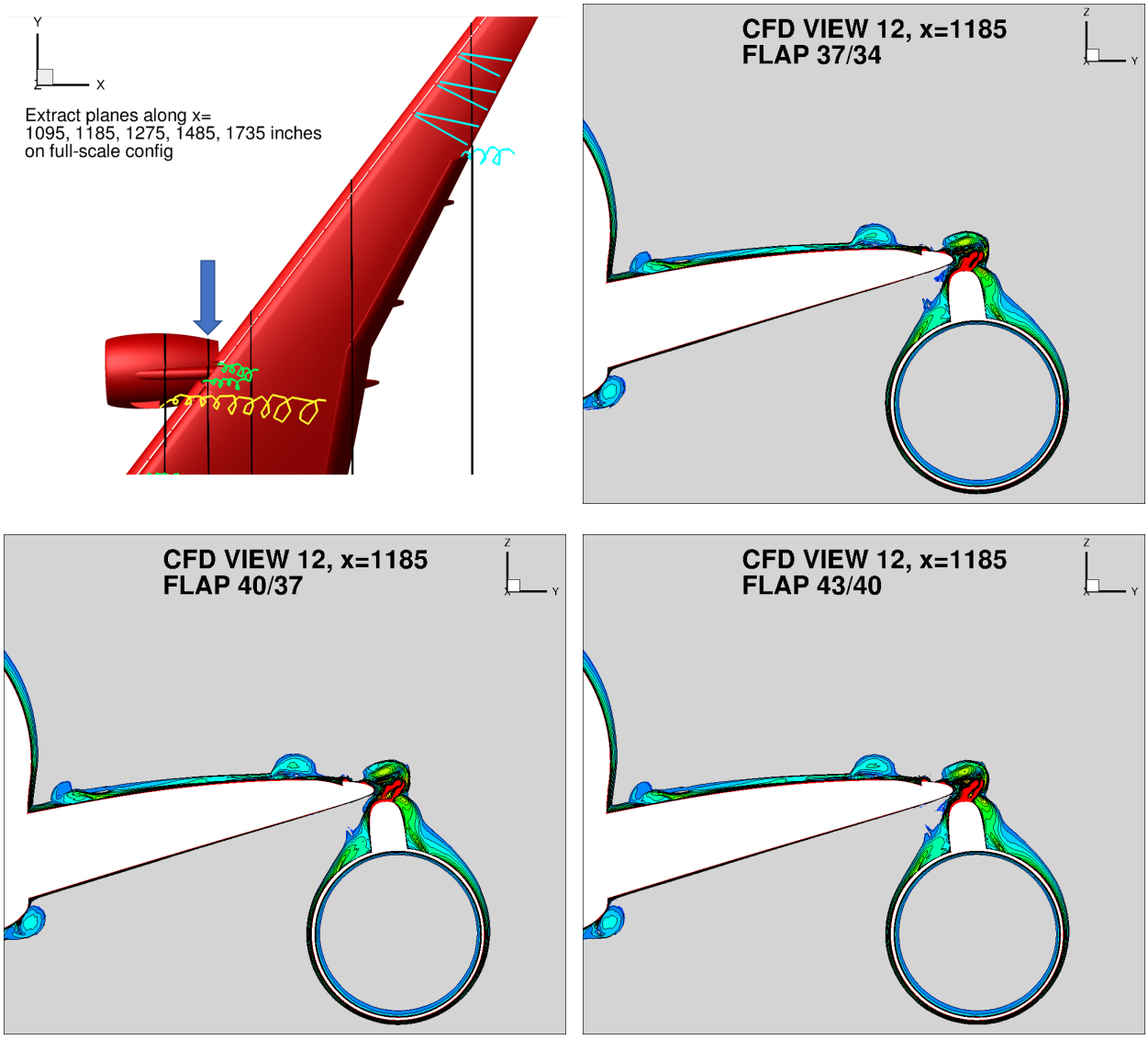

Fig. 16 Nondimensional magnitude of vorticity contours from CFD View 12 [4].

43°/40°. The data presented in this view does not clearly coincide with skin friction distributions depicted in Figure 13.

The data presented in Figures 15, 16, 17, 18, and 19 are well suited to code-to-code comparisons. Unfortunately, the planar views do not permit detailed inferences about the three-dimensional flow structures present around the CRM-HL. Figures 20 and 21 depict Liutex vortex cores [41, 42] colored by angular velocity in CFD View 1 and 5, respectively. The Liutex definition of a vortex is a vector representing rigid rotation about a local axis [41]. Distinguishing shearing motion from rotation facilitates vortex identification and quantitative comparisons of position and angular velocity. The ribbons representing vortex cores in Figures 20 and 21 are generated by seeding stream traces of the Luitex vector field on the standardized planes shown in Figures 15–19. One set of seeding locations, set at the nominal angle of attack, are used to visualize vortex systems across the flap angles. The magnitude of the Liutex vector is proportional to twice the local angular velocity [41, 42]. The orientation of angular velocity follows the right-hand-rule, positive values indicating a counterclockwise rotation and negative values indicating a clockwise rotation.

The top-down perspective of CFD View 1 shown in Figure 20 provides an overview of the vortex sytems from the wing-root to wing tip. In the wing-root region, vortices emanating from the horn and inboard edge of the inboard slat are shown rotating in a counterclockwise direction, while secondary vortices arrising further aft within the

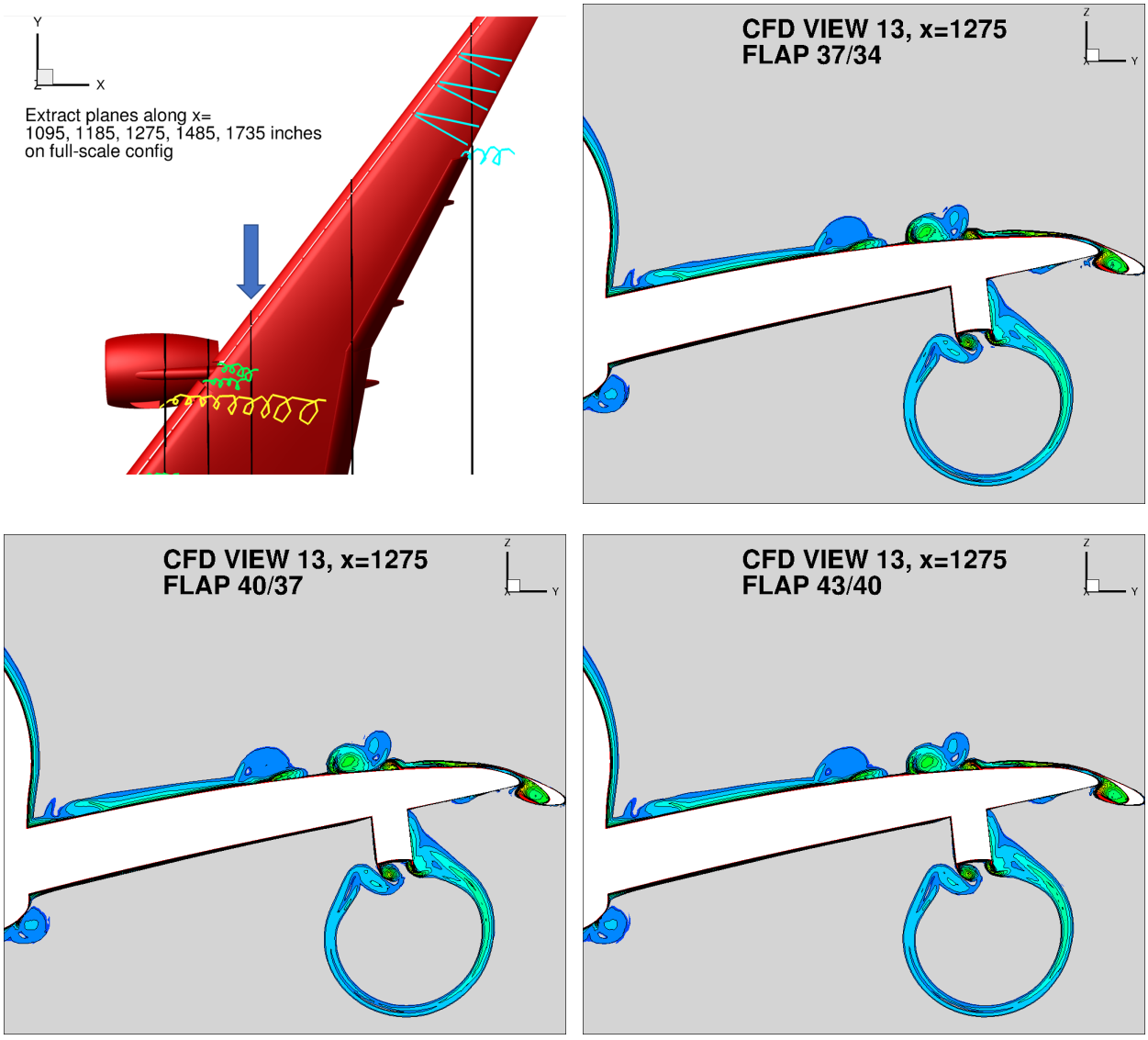

Fig. 17 Nondimensional magnitude of vorticity contours from CFD View 13 [4].

wing-body-junction are counter-rotating in the clockwise direction. The vortices emanating from the nacelle chine and pylon are visualized as spiraling sets of counter-rotating vortices. The vortex cores initiated in the wing-root and nacelle regions have spanwise extensions across the boundary layer on wing's upper surface with diminising angular velocity. This visualization depicts one mechanism that high-energy flows are entrained into boundary layers [38–41]. The imprint of slat bracket wakes are visible in the undulations of the vortex core ribbons above the wing, aft of the outboard slat. The strongest vortex systems visualized are flowing around the nacelle pylon and flap fairings to be the prominent features in the wake region. Vortices with spanwise orientation are also found in the wake region where recirculation occurs within the wake sheet. Figure 20 shows increasing interaction between the nacelle-pylon vortex systems and the boundary layer on the wing's upper surface as the flap settings are increased. The spanwise extension of vortex cores from the nacell-pylon system across the boundary layer begins further forward as the flap settings are increased. The down stream impacts of increasing flap settings are more visible from the persepctive of CFD View 5 shown in Figure 21.

Vortex cores above the flaps in Figure 21 depict significant changes in flow structures as the flap settings are increased. The strength and volume of the vortex system flowing from the wing root past the inboard edge of the inboard

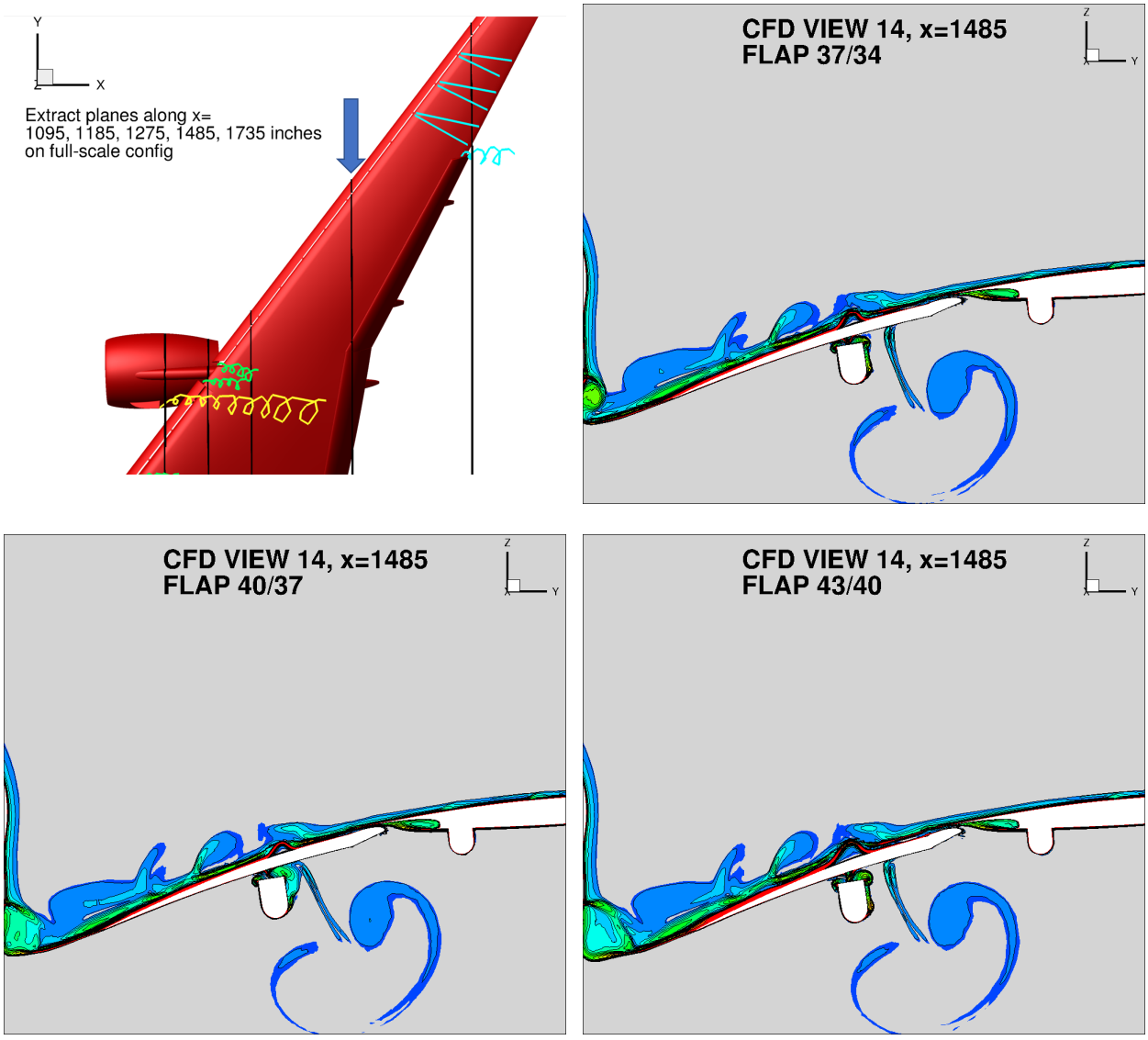

Fig. 18 Nondimensional magnitude of vorticity contours from CFD View 14 [4].

flap diminishes adjacent to the flap trailing edge as the flap angle increases. Associated with the changes to the vortices down stream of the wing root, are the development of spanwise vortices on the inboard flap as the flap settings are increased. The visualization also suggests that the shear flow from the flap cove breaks down the nacelle-chine and nacelle-pylon vortex systems where these features interact. Dynamic changes to the flow around and down stream of the outboard flap are indicated by changes in positions and angular velocities of vortices. These observations compliment the changes in skin friction depicted in Figure 14. As the flap settings are increased, the vortex systems flowing under the wing from the nacelle and flap farings show higher angular velocities and remain narrow farther down stream. Using the Liutex vector field representation for vortex systems, depicted in Figures 20 and 21, reveals insights into the changes in three-dimensional flow structures surrounding the CRM-HL across the flap settings that are not possible through other vortex identification methods [41, 42].

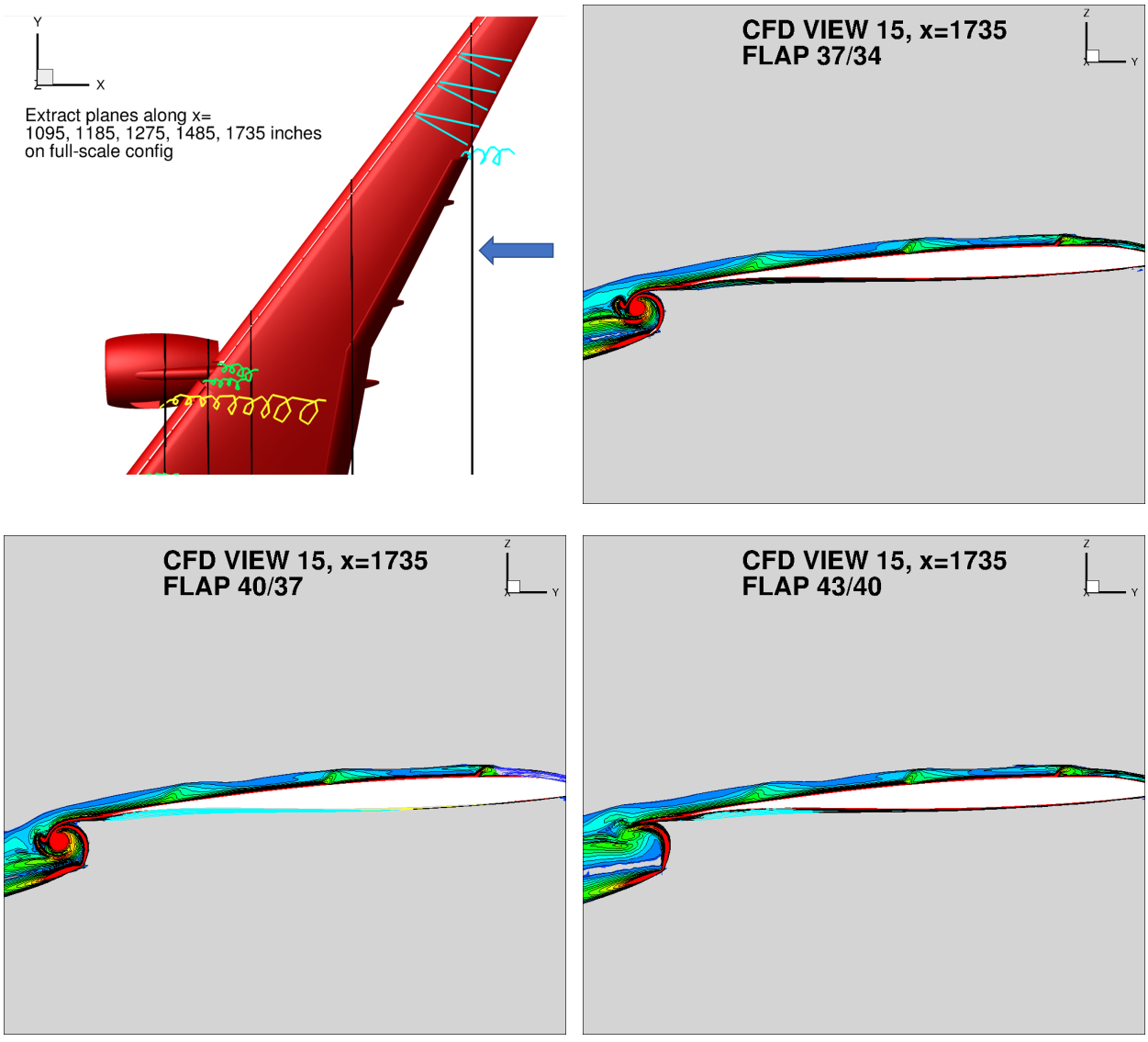

Fig. 19 Nondimensional magnitude of vorticity contours from CFD View 15 [4].

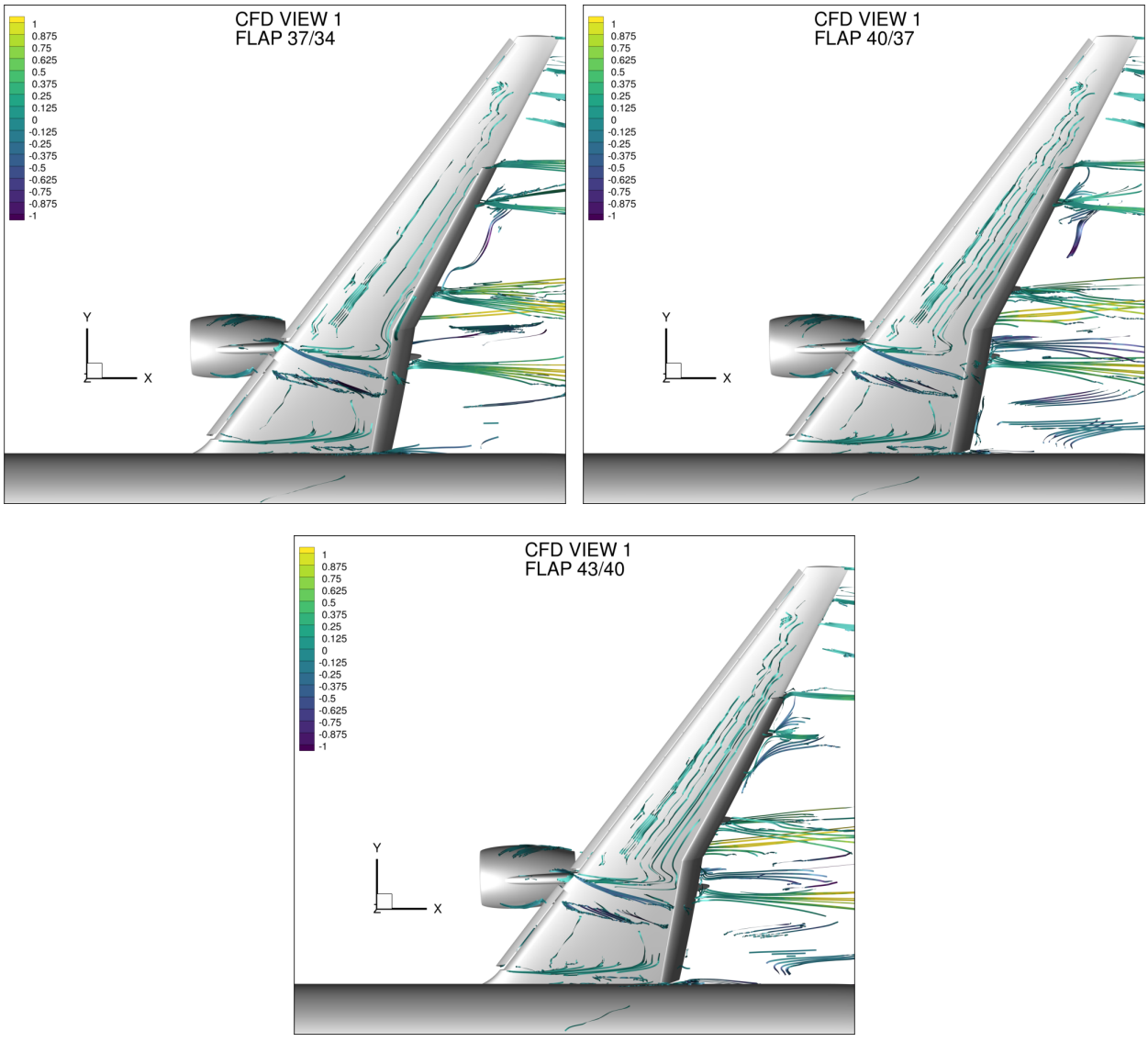

Fig. 20 Off-body vortices visualized with Liutex cores colored by angular velocity from CFD View 1.

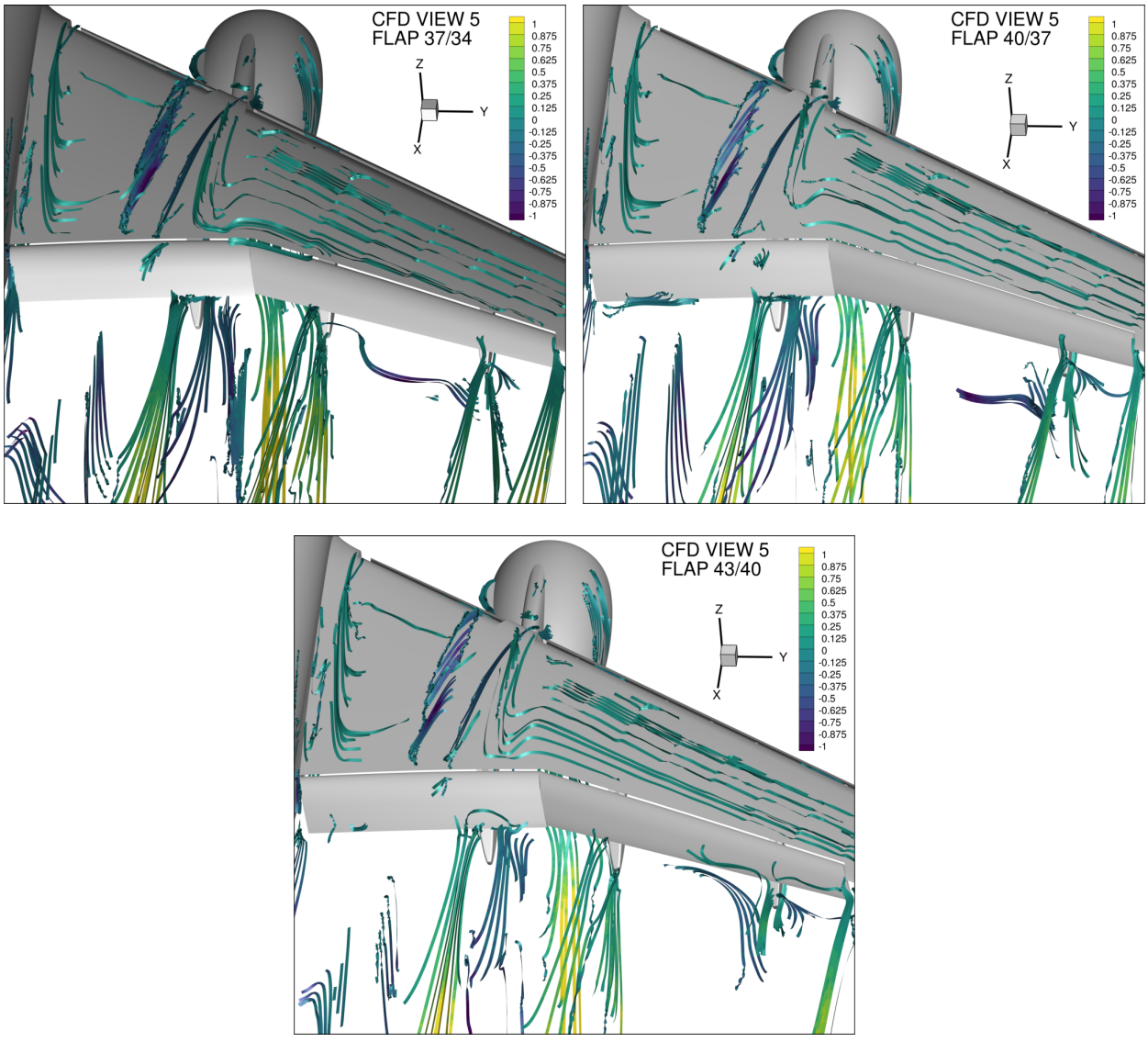

Fig. 21 Off-body vortices visualized with Liutex cores colored by angular velocity from CFD View 5.

E. Convergence

The steady-state RANS solutions in this work have been obtained by reducing the mean flow and turbulence-model residuals to the values shown in Figure 22. The CRM-HL geometry is scaled in inches with a large outer domain, consequently, machine precision for forward solutions is 10^{-9}. The adjoint solutions in this work have been obtained by reducing the mean flow and turbulence-model residuals to the values shown in Figure 23. Consistent iterative convergence of the forward and adjoint problems helps to provide a fair comparion of solutions across the flap settings.

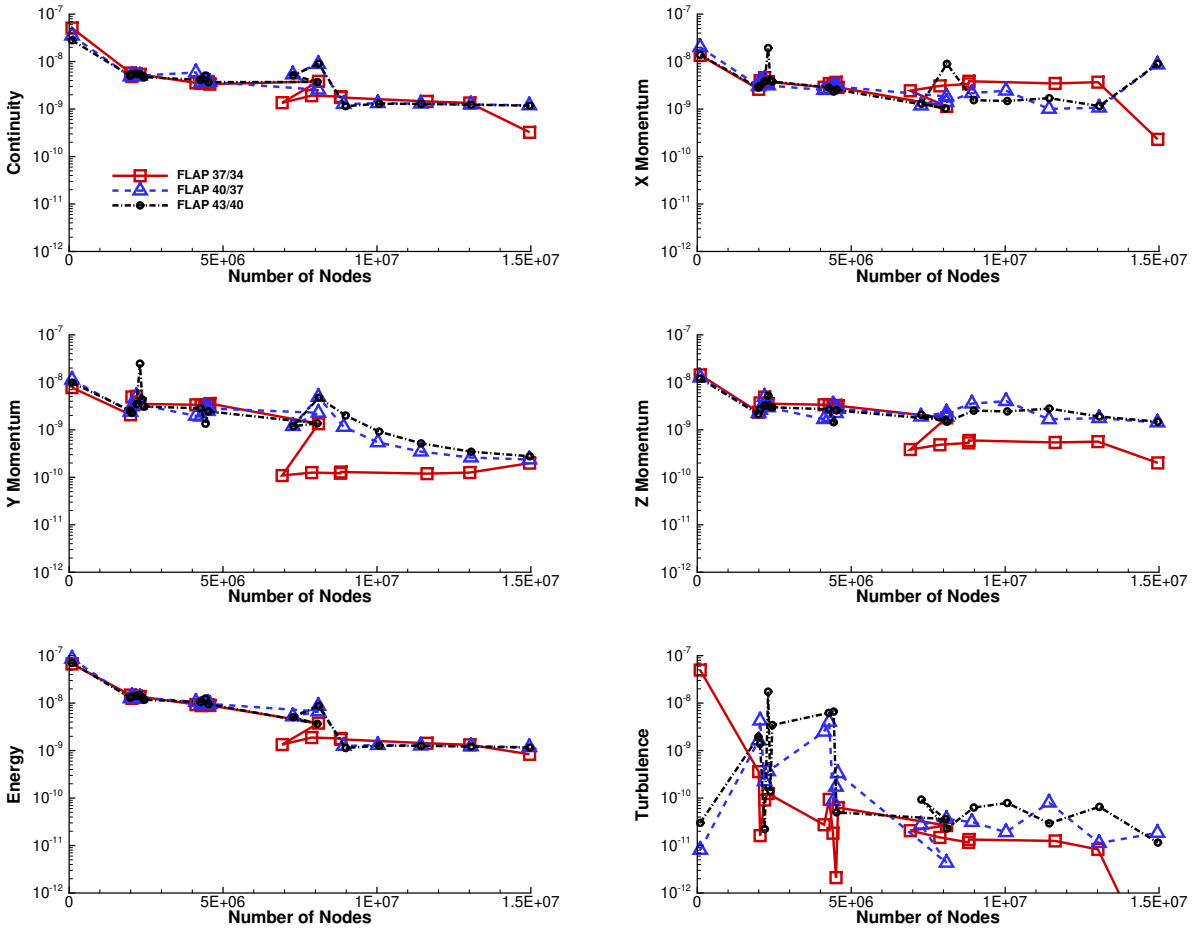

Fig. 22 Final absolute nonlinear residuals for forward solutions obtained on adapted meshes for each flap setting.

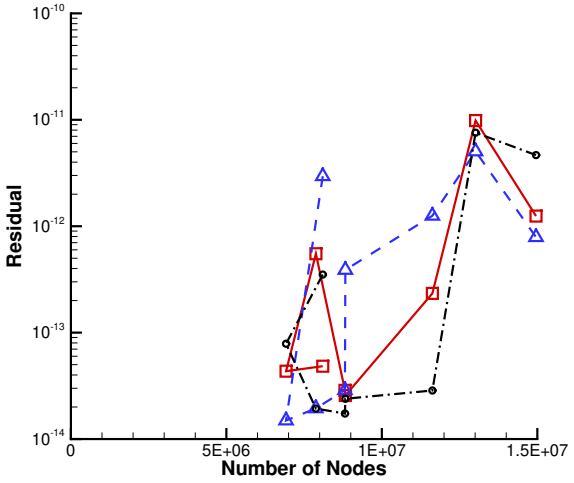

Fig. 23 Final absolute linear residual for adjoint solutions obtained on adapted meshes for each flap setting.

F. Computational Cost

Computational cost is an important factor to monitor in code-to-code comparisons. Table 2 summarizes the total cost of the forward and adjoint solutions. The first author did not record the core-hours needed for mesh generation. This is an aggregious oversight, a sign of *refine*'s maturity, and a missed opportunity to quantify the cost of mesh generation. The first author estimates the total wall time and core-hours used for mesh refinement to be less than 5% of the totals presented for each flap setting. The computations at each flap setting were performed with 10–25 dual socket 8 core 2.60 GHz Intel®E5-2670 Sandybridge (2 x 20MB cache) nodes [43]. Figure 24 depicts the wall-time and core-hours (shown in Standard Billing Units (SBU) [44]) of the forward and adjoint solution calculated at each flap setting. The cost of forward solutions is high where increasing resolution revealed new interactions with geometry and between flow structures that were not present in the converged solution of the prior mesh.

Table 2 Total computational cost in wall time [hours] and Standard Billing Units (SBU) [44].

	Total Wall Time [hours]	Total SBU
Forward Solution		
Flap 37°/34°	81.8	1845.0
Flap 40°/37°	51.0	1124.4
Flap 43°/40°	121.8	2806.7
Adjoint Solution		
Flap 37°/34°	6.0	149.1
Flap 40°/37°	6.5	162.6
Flap 43°/40°	7.3	181.4
Forward + Adjoint Solutions		
Flap 37°/34°	87.8	1994.1
Flap 40°/37°	57.5	1287.1
Flap 43°/40°	129.0	2988.2

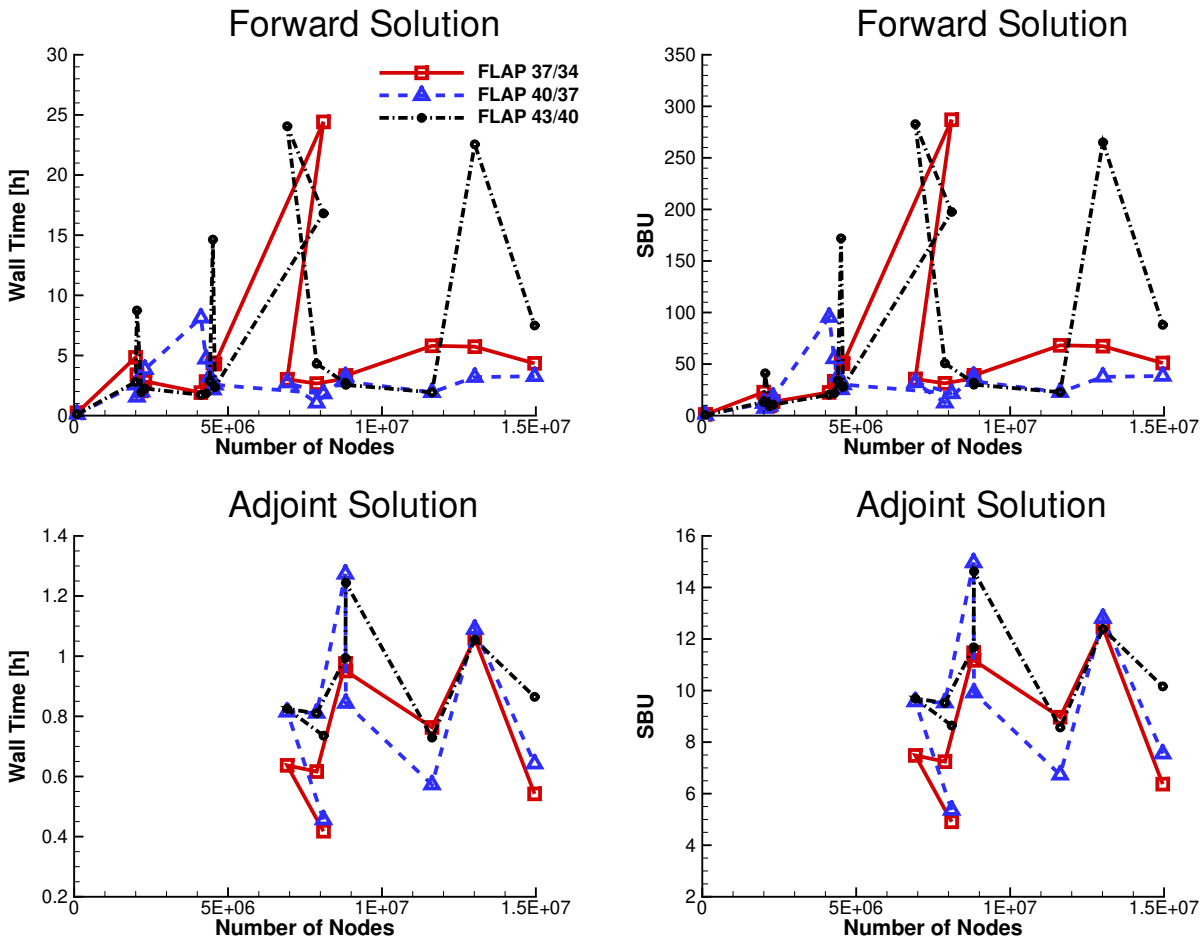

Fig. 24 Computational cost in wall time [hours] and Standard Billing Units (SBU) [44] on adapted meshes for each flap setting.

IV. Summary

An assesment of FUN3D/SFE capabilities pertinent to prediction of force and moment increments for three flap deflections of the CRM-HL at a nominal angle of attack has been completed. The results presented in this work show that while the predicted figures of merit are within 7% of measurements the increments are not well predicted. Predicted surface pressures at eight spanwise locations, skin friction contour plots of the upper surface, and five planes of off-body vorticity magnitude, have been presented to facilitate code-to-code comparison and landmark analysis of flow structures. These detailed data sets show inconsistent discrepancies with measurements across the flap settings. These inconsistencies are consistent with RANS-SA results presented at HLPW-4 and highlight the need for caution in evaluating the predictive power of CFD methods. Visualizations of Liutex vortex cores colored by angular velocity are shown as a possibly path forward for quantitative analysis of three-dimensional vortex systems prelevant in aeronautics.

Acknowledgments

This research was sponsored by the NASA Revolutionary Computational Aerosciences (RCA) Transformational Tools and Technologies (TTT) Project of the Transformative Aeronautics Concepts Program under the Aeronautics Research Mission Directorate.

References

[1] Lin, J. C., Melton, L. P., Viken, S. A., Andino, M. Y., Koklu, M., Hannon, J. A., and Vatsa, V. N., "Development of the High Lift Common Research Model for Wind Tunnel Testing: An Active Flow Control Perspective," AIAA Paper 2017–319, 2017. doi:10.2514/6.2017-0319.

[2] Lacy, D. S., and Clark, A. M., "Definition of Initial Landing and Takeoff Reference Configurations for the High Lift Common Research Model (CRM-HL)," AIAA Paper 2020–2771, 2020. doi:10.2514/6.2020-2771.

[3] Evans, A., Lacy, D., Smith, I., and Rivers, M., "Test Summary of the NASA Semi-Span High-Lift Common Research Model at the QinetiQ 5-Metre Low-Speed Wind Tunnel," AIAA Paper 2020–2770, 2020. doi:10.2514/6.2020-2770.

[4] "Test Cases," , April 2022. URL `https://hiliftpw.larc.nasa.gov/Workshop4/index.html`.

[5] "NASA Common Research Model," , 2022. URL `https://commonresearchmodel.larc.nasa.gov/2012/01/19/hello-world-2/`.

[6] Kleb, B., Park, M. A., Wood, W. A., Bibb, K. L., Thompson, K. B., Gomez, R. J., III, and Tesch, S. H., "Sketch-to-Solution: An Exploration of Viscous CFD with Automatic Grids," AIAA Paper 2019–2948, 2019. doi:10.2514/6.2019-2948.

[7] Kleb, B., Schoenenberger, M., Korzun, A. M., and Park, M. A., "Sketch-to-Solution: A Case Study in RCS Aerodynamic Interaction," AIAA Paper 2020–673, 2020. doi:10.2514/6.2020-0673.

[8] Wood, S. L., Anderson, W. K., Park, M. A., Balan, A., Karman, S., and Jacobson, K. E., "Reynolds-Averaged Navier-Stokes Computations of the NASA Juncture Flow Model Using Expert-Crafted and Adapted Grids," AIAA Paper 2020-2751, 2020.

[9] Balan, A., Park, M. A., Wood, S. L., Anderson, W. K., and Jacobson, K. E., "Angle-of-Attack Sweep with Mesh Adaptation for High-Lift Configurations," AIAA Paper 2022–218, 2022. doi:10.2514/6.2022-0218.

[10] Loseille, A., and Alauzet, F., "Continuous Mesh Framework Part I: Well-Posed Continuous Interpolation Error," *SIAM Journal on Numerical Analysis*, Vol. 49, No. 1, 2011, pp. 38–60. doi:10.1137/090754078.

[11] Alauzet, F., and Loseille, A., "A Decade of Progress on Anisotropic Mesh Adaptation for Computational Fluid Dynamics," *Computer-Aided Design*, Vol. 72, 2016, pp. 13–39. doi:10.1016/j.cad.2015.09.005, 23rd International Meshing Roundtable Special Issue: Advances in Mesh Generation.

[12] Park, M. A., and Darmofal, D. L., "Parallel Anisotropic Tetrahedral Adaptation," AIAA Paper 2008–917, 2008.

[13] Loseille, A., Dervieux, A., Frey, P. J., and Alauzet, F., "Achievement of Global Second Order Mesh Convergence for Discontinuous Flows with Adapted Unstructured Meshes," AIAA Paper 2007–4186, 2007. doi:10.2514/6.2007-4186.

[14] Alauzet, F., and Frazza, L., "Feature-Based and Goal-Oriented Anisotropic Mesh Adaptation for RANS Applications in Aeronautics and Aerospace," *Journal of Computational Physics*, Vol. 439, 2021, p. 110340. doi:10.1016/j.jcp.2021.110340.

[15] Galbraith, M. C., Caplan, P. C., Carson, H. A., Park, M. A., Balan, A., Anderson, W. K., Michal, T., Krakos, J. A., Kamenetskiy, D. S., Loseille, A., Alauzet, F., Frazza, L., and Barral, N., "Verification of Unstructured Grid Adaptation Components," *AIAA Journal*, Vol. 58, No. 9, 2020, pp. 3947–3962. doi:10.2514/1.J058783.

[16] Park, M. A., Balan, A., Clerici, F., Alauzet, F., Loseille, A., Kamenetskiy, D. S., Krakos, J. A., Michal, T., and Galbraith, M. C., "Verification of Viscous Goal-Based Anisotropic Mesh Adaptation," AIAA Paper 2021-1362, 2021. doi:10.2514/6.2021-1362.

[17] *FUN3D Fully Unstructured Navier-Stokes*, NASA, Nov. 2019. URL `https://fun3d.larc.nasa.gov/`.

[18] Anderson, W. K., Newman, J. C., and Karman, S. L., "Stabilized Finite Elements in FUN3D," *Journal of Aircraft*, Vol. 55, No. 2, 2018, pp. 696–714. doi:10.2514/1.C034482.

[19] Brooks, A. N., and Hughes, T. J. R., "Streamline Upwind/Petrov-Galerkin Formulation for Convection Dominated Flows with Particular Emphasis on Incompressible Navier-Stokes Equations," *Computer Methods in Applied Mechanics and Engineering*, Vol. 32, No. 1–3, 1982, pp. 199–259. doi:10.1016/0045-7825(82)90071-8.

[20] Shakib, F., Hughes, T. J. R., and Johan, Z., "A New Finite-Element Formulation for Computational Fluid Dynamics: X. The Compressible Euler and Navier-Stokes Equations," *Computer Methods in Applied Mechanics and Engineering*, Vol. 89, No. 1–3, 1991, pp. 141–219. doi:10.1016/0045-7825(91)90041-4.

[21] Allmaras, S. R., Johnson, F. T., and Spalart, P. R., "Modifications and Clarifications for the Implementation of the Spalart-Allmaras Turbulence Model," *Seventh International Conference on Computational Fluid Dynamics (ICCFD7)*, 2012.

[22] Anderson, W. K., Wood, S. L., and Allmaras, S. R., "An Initial Exploration of Improved Numerics within the Guidelines of the Negative Spalart-Allmaras Turbulence Model," Technical Memorandum 2019-220429, 2019-11 2019.

[23] Holst, K. R., Glasby, R. S., Erwin, J. T., Stefanski, D. L., and Coder, J. G., "High-Order Shock Capturing Techniques using HPCMP CREATE™-AV Kestrel," AIAA Paper 2019–1345, 2019. doi:10.2514/6.2019-1345.

[24] Balan, A., Park, M. A., and Anderson, W. K., "Adjoint-based Anisotropic Mesh Adaptation for a Stabilized Finite-Element Flow Solver," AIAA Paper 2019–2949, 2019.

[25] Balan, A., Park, M. A., Wood, S. L., and Anderson, W. K., "Verification of Anisotropic Mesh Adaptation for Complex Aerospace Applications," AIAA Paper 2020–675, 2020. doi:10.2514/6.2020-0675.

[26] Saad, Y., *Iterative Methods for Sparse Linear Systems*, 2nd ed., Society for Industrial and Applied Mathematics, Philadelphia, PA, USA, 2003.

[27] Anderson, W. K., Wood, S. L., and Jacobson, K. E., "Node Numbering for Stabilizing Preconditioners Based on Incomplete LU Decomposition," AIAA Paper 2020–3022, 2020. doi:10.2514/6.2020-3022.

[28] Anderson, W. K., and Bonhaus, D. L., "Airfoil Design on Unstructured Grids for Turbulent Flows," *AIAA Journal*, Vol. 37, No. 2, 1999, pp. 185–191. doi:10.2514/2.712, URL https://doi.org/10.2514/2.712.

[29] Wood, S. L., Jacobson, K. E., Jones, W. T., and Anderson, W. K., "Sparse Linear Algebra Toolkit for Computational Aerodynamics," AIAA Paper 2020–317, 2020. doi:10.2514/6.2020-0317.

[30] Haimes, R., and Drela, M., "On The Construction of Aircraft Conceptual Geometry for High-Fidelity Analysis and Design," AIAA Paper 2012–683, 2012. doi:10.2514/6.2012-683.

[31] Haimes, R., and Dannenhoffer, J. F., III, "The Engineering Sketch Pad: A Solid-Modeling, Feature-Based, Web-Enabled System for Building Parametric Geometry," AIAA Paper 2013–3073, 2013. doi:10.2514/6.2013-3073.

[32] Dannenhoffer, J. F., III, "OpenCSM: An Open-Source Constructive Solid Modeler for MDAO," AIAA Paper 2013–701, 2013. doi:10.2514/6.2013-701.

[33] Haimes, R., and Dannenhoffer, J. F., III, "EGADSlite: A Lightweight Geometry Kernel for HPC," AIAA Paper 2018–1401, 2018. doi:10.2514/6.2018-1401.

[34] Loseille, A., Dervieux, A., and Alauzet, F., "Fully anisotropic goal-oriented mesh adaptation for 3D steady Euler equations," *Journal of Computational Physics*, Vol. 229, No. 8, 2010, pp. 2866 – 2897. doi:https://doi.org/10.1016/j.jcp.2009.12.021, URL http://www.sciencedirect.com/science/article/pii/S0021999109007001.

[35] Peraire, J., Vahdati, M., Morgan, K., and Zienkiewicz, O. C., "Adaptive Remeshing for Compressible Flow Computations," *Journal of Computational Physics*, Vol. 72, No. 2, 1987, pp. 449–466. doi:10.1016/0021-9991(87)90093-3.

[36] Peraire, J., Peirò, J., and Morgan, K., "Adaptive Remeshing for Three-Dimensional Compressible Flow Computations," *Journal of Computational Physics*, Vol. 103, No. 2, 1992, pp. 269–285. doi:10.1016/0021-9991(92)90401-J.

[37] Kamenetskiy, D. S., Krakos, J. A., Michal, T., Clerici, F., Alauzet, F., Loseille, A., Park, M. A., Wood, S., Balan, A., and Galbraith, M. C., "Anisotropic Goal-Based Mesh Adaptation Metric Clarification and Development," AIAA Paper 2022-1245, 2022. doi:10.2514/6.2022-1245.

[38] Alin, N., and Fureby, C., "Large Eddy Simulation of Junction Vortex Flows," AIAA Paper 2008–668, 2008.

[39] McKenna, C. K., Rice, B. E., Bisek, N. J., Peltier, S. J., and Hofferth, J. W., "Reynolds Number Effects on Secondary Motion in Corner Flow Boundary Layers," AIAA Paper 2019–3342, 2019.

[40] McKenna, C. K., Rice, B. E., Bisek, N. J., Peltier, S. J., and Hofferth, J. W., "Mach Number Effects on Secondary Motion in Corner Flow Boundary Layers," AIAA Paper 2020–0835, 2020.

[41] Liu, C., Xu, H., Cai, X., and Gao, Y., *Liutex and Its Applications in Turbulence Research*, Academic Press, 2020, pp. 1–436.

[42] Liu, C., "Liutex and Third Generation of Vortex Identification Methods," *Liutex and Third Generation of Vortex Definition and Identification*, Springer, 2021, pp. 3–36.

[43] "Intel® Xeon® Processor E5-2670 (20M Cache, 2.60 GHz, 8.00 GT/s Intel® QPI) Product Specifications," , 2017. URL https://ark.intel.com/products/64595/Intel-Xeon-Processor-E5-2670-20M-Cache-2_60-GHz-8_00-GTs-Intel-QPI.

[44] "NASA High-End Computing: Standard Billing Units," , 2022. URL https://hec.nasa.gov/user/policies/sbus.html.